






Rapid northern hemisphere ice sheet melting during the penultimate deglaciation

Heather M. Stoll ¹✉, Isabel Cacho², Edward Gasson^{3,4}, Jakub Sliwinski^{1,5}, Oliver Kost ¹, Ana Moreno ⁶, Miguel Iglesias ⁷, Judit Torner², Carlos Perez-Mejias⁸, Negar Haghipour^{1,9}, Hai Cheng ^{8,10} & R. Lawrence Edwards^{10,11}

The rate and consequences of future high latitude ice sheet retreat remain a major concern given ongoing anthropogenic warming. Here, new precisely dated stalagmite data from NW Iberia provide the first direct, high-resolution records of periods of rapid melting of Northern Hemisphere ice sheets during the penultimate deglaciation. These records reveal the penultimate deglaciation initiated with rapid century-scale meltwater pulses which subsequently trigger abrupt coolings of air temperature in NW Iberia consistent with freshwater-induced AMOC slowdowns. The first of these AMOC slowdowns, 600-year duration, was shorter than Heinrich 1 of the last deglaciation. Although similar insolation forcing initiated the last two deglaciations, the more rapid and sustained rate of freshening in the eastern North Atlantic penultimate deglaciation likely reflects a larger volume of ice stored in the marine-based Eurasian Ice sheet during the penultimate glacial in contrast to the land-based ice sheet on North America as during the last glacial.

¹Department of Earth Sciences, ETH Zürich, Zurich, Switzerland. ²Grup de Recerca Consolidat en Geociències Marines, Departament de Dinàmica de la Terra i de l'Oceà, Universitat de Barcelona, Barcelona, Spain. ³School of Geographical Sciences, University of Bristol, Bristol, UK. ⁴Earth and Environmental Sciences, University of Exeter, Exeter, UK. ⁵Currently at School of Earth and Environmental Sciences, University of St. Andrews, St. Andrews, UK. ⁶Department of Geoenvironmental Processes and Global Change, Pyrenean Institute of Ecology-CSIC, Zaragoza, Spain. ⁷Department of Geology, University of Oviedo, Oviedo, Spain. ⁸Institute of Global Environmental Change, Xi'an Jiaotong University, Xi'an, China. ⁹Laboratory for Ion Beam Physics, Department of Physics, ETH Zurich, Switzerland. ¹⁰Department of Earth and Environmental Sciences, University of Minnesota, Minneapolis, USA. ¹¹School of Geography, Nanjing Normal University, Nanjing 210023, China. ✉email: heather.stoll@erdw.ethz.ch

During glacial terminations, retreating ice sheets release large meltwater fluxes into the ocean. This leads to rising sea level and can initiate strong climate feedbacks when sufficiently large meltwater fluxes reach regions of deepwater formation in the North Atlantic. These ocean-atmosphere interactions, together with associated ocean CO₂ release, operate as strong and rapid amplifiers of the original orbital induced insolation change. The rapid retreat of ice sheets which yields high meltwater fluxes, can be caused by marine ice sheet instability, ice sheet saddle collapse and marine ice cliff failure^{1,2}. While the timing and associated deglacial feedbacks have been extensively studied for the last deglaciation (Termination I, TI)³, knowledge of the insolation thresholds, rate of ice sheet melting, and feedback sequence of previous terminations is more limited due to the lack of direct absolute chronology for ice retreat and deglacial warming. Some studies suggest that the sequence of millennial feedbacks may be different in previous terminations^{4,5}. The penultimate deglaciation, Termination II (TII), is of particular interest because orbital boundary conditions were different, and the termination was followed by an interglacial with a +1.2 to 5.3 m sea level highstand - suggesting both Greenland and Antarctic ice sheets retreated further than during TI⁶, despite similar highs in atmospheric CO₂⁷. To fully understand the last interglacial highstand, clear knowledge of the ice sheets melting time and retreat rates during TII is needed^{8,9}.

Water stored in high latitude ice sheets has a $\delta^{18}\text{O}$ lower than the mean ocean, meaning the deglacial melting of the Northern Hemisphere (NH) ice sheets lowers the $\delta^{18}\text{O}$ of the surface ocean ($\delta^{18}\text{O}_{\text{sw}}$). For regions proximal to release of glacial meltwater, such as the North Atlantic, the rate of $\delta^{18}\text{O}_{\text{sw}}$ depletion and freshening can exceed the global average^{10,11}, which has been useful in diagnosing meltwater routes during TI^{12–14}. We propose that the evolution of the North Atlantic $\delta^{18}\text{O}_{\text{sw}}$ can be recorded in coastal European speleothems through the transfer of the $\delta^{18}\text{O}_{\text{sw}}$ signal of the ocean moisture source to the $\delta^{18}\text{O}$ of rainfall, and thereby the $\delta^{18}\text{O}$ of dripwater¹⁵ from which the speleothem is formed. We report on the North Iberian Speleothem Archive (NISA) from caves within 10 km of the Atlantic coast (Fig. 1) at coastal elevation (<70 m above sea level), directly adjacent to the main moisture source region in the eastern North Atlantic. We employ speleothems spanning the last 25 ky to evaluate the $\delta^{18}\text{O}$ and $\delta^{13}\text{C}$ proxy relationships against independent records of regional temperature and $\delta^{18}\text{O}_{\text{sw}}$. The analysis of speleothems covering TI and TII from the same caves and same proxy indicators provides, by the first time, the opportunity to unambiguously compare the timing and rate of the last two deglaciations on an absolute ²³⁰Th chronology, with rates further refined by annual layer counting in TII. We show that the NISA record provides a unique opportunity to directly link the impact of rapid freshening of the North Atlantic on regional atmospheric temperatures, using the same archive, in order to test mechanisms for deglacial feedbacks.

Results and discussion

Controls on the $\delta^{18}\text{O}$ and $\delta^{13}\text{C}$ of NISA speleothems. Using six stalagmites spanning the last 25 ky to generate a composite splice speleothem $\delta^{18}\text{O}$ record (Methods; Supplementary Figs. 1 and 2), we test the relationship between the speleothem $\delta^{18}\text{O}$ and independent $\delta^{18}\text{O}_{\text{sw}}$ estimates from foraminifera in North Atlantic marine sediment cores (Supplementary Fig. 3).

We find that throughout the last 25 ka, where both marine and speleothem records rely on independent absolute chronologies, $\delta^{18}\text{O}_{\text{NISA}}$ exhibits an unusually close correlation with the $\delta^{18}\text{O}_{\text{sw}}$ in the eastern North Atlantic Ocean. The $\delta^{18}\text{O}_{\text{NISA}}$ is most strongly correlated (r^2 of 0.91) with the $\delta^{18}\text{O}_{\text{sw}}$ on the Irish Margin¹⁶ and a low standard error indicates a consistent

relationship throughout the deglaciation despite the potential for variation in atmospheric and surface ocean boundary conditions (Fig. 2, Supplementary Table 1). Strong correlation is also attained for the $\delta^{18}\text{O}_{\text{sw}}$ of the S. Iberian Margin¹⁷ and W. Iberian Margin¹⁸ (Fig. 2, Supplementary Table 1), as expected given the southward flowing eastern boundary current from the Irish margin along the Iberian margin and via the Atlantic Jet surface water flow through the Straits of Gibraltar¹⁹. The latter regions $\delta^{18}\text{O}_{\text{sw}}$ are also closely correlated with the Irish margin $\delta^{18}\text{O}_{\text{sw}}$ (Supplementary Table 2) and show no systematic changes in the $\delta^{18}\text{O}_{\text{sw}}$ gradients (Supplementary Fig. 3). A HadCM3 model of the early phases of the TI deglaciation, simulating meltwater based on ICE6G ice sheet evolution and drainage routing (meltwater ~45% from EIS and 55% from the NAIS), yields similar spatial pattern of meltwater-induced salinity anomaly. Low salinity is concentrated in the North Atlantic north of 40°N, including the Irish Margin¹⁰ and extending further southward due to eastern boundary current²⁰ along the Iberian Peninsula, NW coast of Africa, and into the Alboran Sea (Fig. 1). The strong relationship between $\delta^{18}\text{O}_{\text{NISA}}$ and the proximal surface ocean $\delta^{18}\text{O}_{\text{sw}}$ is not observed in Mediterranean region speleothems over TI (Supplementary Table 3), likely due to additional hydrological effects^{21–23}.

Several factors may contribute to the coherence between $\delta^{18}\text{O}_{\text{NISA}}$ and the $\delta^{18}\text{O}_{\text{sw}}$ of the proximal ocean. Our analysis of all precipitation events in Northern Spain at a station <100 km west of the cave site in 2015–2016, shows that the majority of rainfall events in this region derive from oceanic moisture uptake in the easternmost North Atlantic ocean proximal to the Iberian Peninsula, especially north of Iberia (Fig. 2d). The high east-west topographic barrier of the Pyrenees and Cantabrian mountains of Northern Spain likely contributes both to the modern dominance of this northern proximal ocean moisture source and the stability of this moisture source over time. The location of caves at coastal elevation, directly adjacent to the main Atlantic moisture source region, minimizes the isotopic distillation between the moisture source area and the cave site. The imprint of such distillation on speleothem $\delta^{18}\text{O}$ from European caves increases with their increasing inland distance and elevation²⁴; and temperature modulates this distillation so that temperature rather than the $\delta^{18}\text{O}_{\text{sw}}$ of moisture source, becomes the dominant influence on $\delta^{18}\text{O}_{\text{NISA}}$ in central Europe^{25,26}. In our NW Iberian cave locations, rainfall monitoring shows that the slight decrease in rainfall $\delta^{18}\text{O}$ with decreasing temperature²⁷ appears of similar magnitude but opposite sign as the temperature-dependent fractionation between dripwater and calcite in the cave, leaving the $\delta^{18}\text{O}_{\text{sw}}$ of the Atlantic moisture source as the principal variable expressed in the stalagmites. We propose that the $\delta^{18}\text{O}_{\text{sw}}$ - $\delta^{18}\text{O}_{\text{NISA}}$ relationship identified in TI remained stable over TII.

Additionally, we confirm that over TI, the $\delta^{13}\text{C}_{\text{NISA}}$ in stalagmites from our caves varies inversely with regional temperature records from marine archives (Methods, Fig. 3; Supplementary Fig. 4), matching millennial variations in SST despite potential deviations in marine ¹⁴C chronology due to variation in surface ocean reservoir ages²⁸ and the potential for alkenones of differing production ages to be deposited together²⁹. Similar temporal correlation between temperature and $\delta^{13}\text{C}$ during marine isotope stages 3 and 4 has been observed in speleothems from the Atlantic coastal region of France³⁰. We conclude that the main trends are attributable to the carbon isotope signature acquired through rain equilibration with soil gas and bedrock dissolution, rather than in-cave processes such as prior calcite precipitation (Methods). Multiproxy process modeling suggests that this correlation arises because higher temperature strongly increases vegetation productivity in this biogeographic regime, enhancing soil CO₂ production and

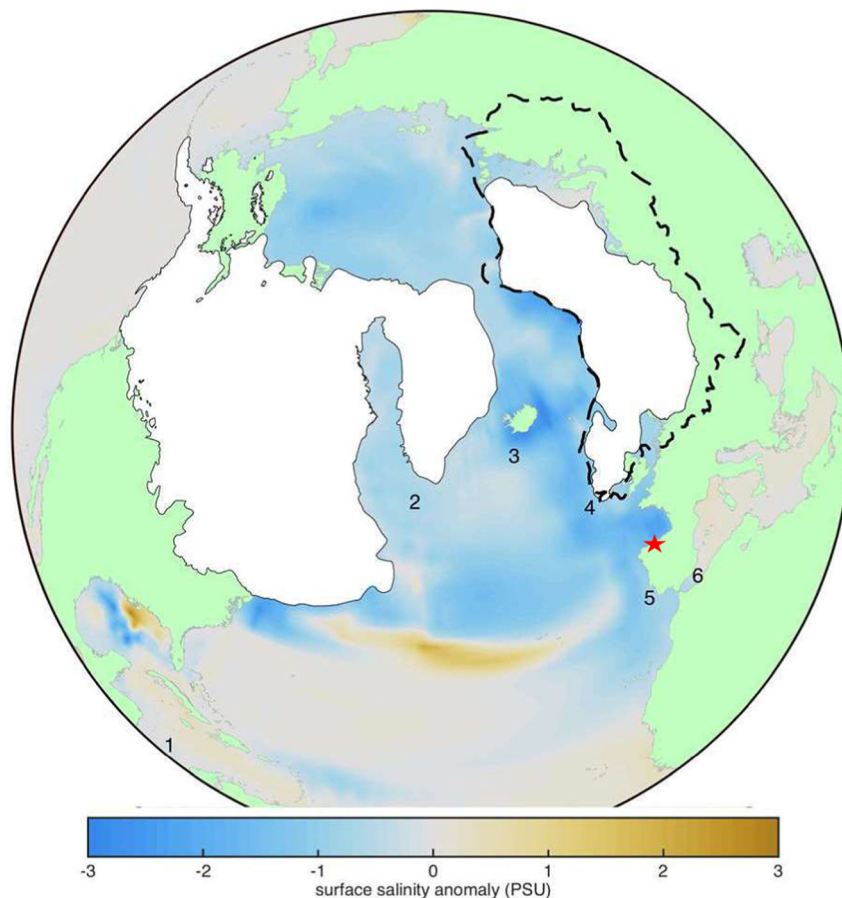


Fig. 1 Northern hemisphere ice sheets and site locations. The distribution of North American Ice Sheet (NAIS) and Eurasian Ice Sheet (EIS) during the LGM (white coverage, after¹⁰⁸) and the maximum extent of EIS glacial deposits prior to the last glacial cycle (black dashed lines, after⁴⁶). Color scale over the ocean depicts the distribution of marine salinity anomalies at 16 ka resulting from a 3000 ky simulation with meltwater derived 45% from the EIS and 55% from the NAIS delivered to appropriate coastal outlets and leading to a 20% AMOC slowdown¹⁰. NW Iberian cave site (red star), and locations discussed: 1 Western Caribbean Site (ODP 999); 2 Eirik drift (MD03-2664); 3 North Atlantic Sites (ODP 983 and 984); 4 Irish Margin site (MD01-2461); 5 W Iberian Margin MD99-2334K; MD01-2343; MD01-2444; MD95-2042, MD95-2040; SHAK06-5K); 6 S Iberian Margin (ODP 976 and 977; MD95-2043).

oversupply of CO_2 to karst waters, both factors which produce more negative $\delta^{13}\text{C}$ in speleothems ($\delta^{13}\text{C}_{\text{speleo}}$)³¹. We infer that the specific slope of the temperature vs $\delta^{13}\text{C}_{\text{NISA}}$ relationships may be specific to a given cave systems and host lithology, and may be sensitive to the degree of smoothing of millennial-scale changes which is affected by the speleothem growth rate and the years aggregated in each drilling increment.

NISA speleothem records spanning TII. In the same coastal cave systems, we document the evolution of $\delta^{18}\text{O}_{\text{NISA}}$ and $\delta^{13}\text{C}_{\text{NISA}}$ over TII as indicators of $\delta^{18}\text{O}_{\text{sw}}$ and temperature, respectively. Three ^{230}Th -dated NISA stalagmites replicate the main features of the TII deglaciation between 135 and 129 ka (Fig. 4a). Annual countable fluorescent banding in stalagmite Garth (Supplementary Figs. 5 and 6) additionally provides a precise estimation of the rate of the main $\delta^{18}\text{O}_{\text{NISA}}$ transitions. The record from stalagmite Garth extends to 112 ka BP and provides further context for the deglaciation, albeit with slowed growth and lower resolution between 127.5 and 122.5 ka. We assess the potential effect of in-cave processes such as PCP on the isotope records to focus on the most robust proxy trends (Methods, Supplementary Figs. 7–10) Given the correlation between $\delta^{18}\text{O}_{\text{NISA}}$ and marine microfossil records of $\delta^{18}\text{O}_{\text{sw}}$ from west and south Iberia in TI (Fig. 1), we tune marine sediment age

models to speleothem chronology by synchronizing the major freshening associated with deglacial ice melting and some key temperature events (Methods, Supplementary Figs. 11–15).

$\delta^{13}\text{C}_{\text{NISA}}$ records the stepped deglacial warming from 134 to 128 ka, punctuated by millennial cooling events, while $\delta^{18}\text{O}_{\text{NISA}}$ records the deglacial freshening of the eastern North Atlantic beginning 135.7 ka (Fig. 4a). The subsequent descent into the last glacial cycle is also reflected in the increase in $\delta^{18}\text{O}_{\text{NISA}}$ after 122 ka and persistent cooling in $\delta^{13}\text{C}_{\text{NISA}}$ after 118 ka which suggest temperatures similar to the PGM by 112 ka. The annual layer counted chronology in many sections of stalagmite Garth resolves significant centennial to millennial scale variations in both the rate of eastern North Atlantic freshening ($\delta^{18}\text{O}_{\text{NISA}}$) and its relationship with regional warming ($\delta^{13}\text{C}_{\text{NISA}}$) (Fig. 4b).

Two large freshening pulses characterize the TII onset (MWPTII-A and MWPTII-B, Fig. 4b). Following previous studies³², we infer that the addition of meltwater is the main driver of rapid deglacial freshening and declines in the $\delta^{18}\text{O}_{\text{sw}}$ in the eastern North Atlantic. Both abrupt freshening pulses began during a period of rapid warming, then, after several decades of rapid freshening, temperatures cooled rapidly, consistent with freshening-induced AMOC slowdown (Fig. 4b). Yet despite cooling, the freshening rate remained high for nearly a century during both events. Following the first period of rapid meltwater release (MWPTII-A), a local freshwater $\delta^{18}\text{O}$ anomaly was

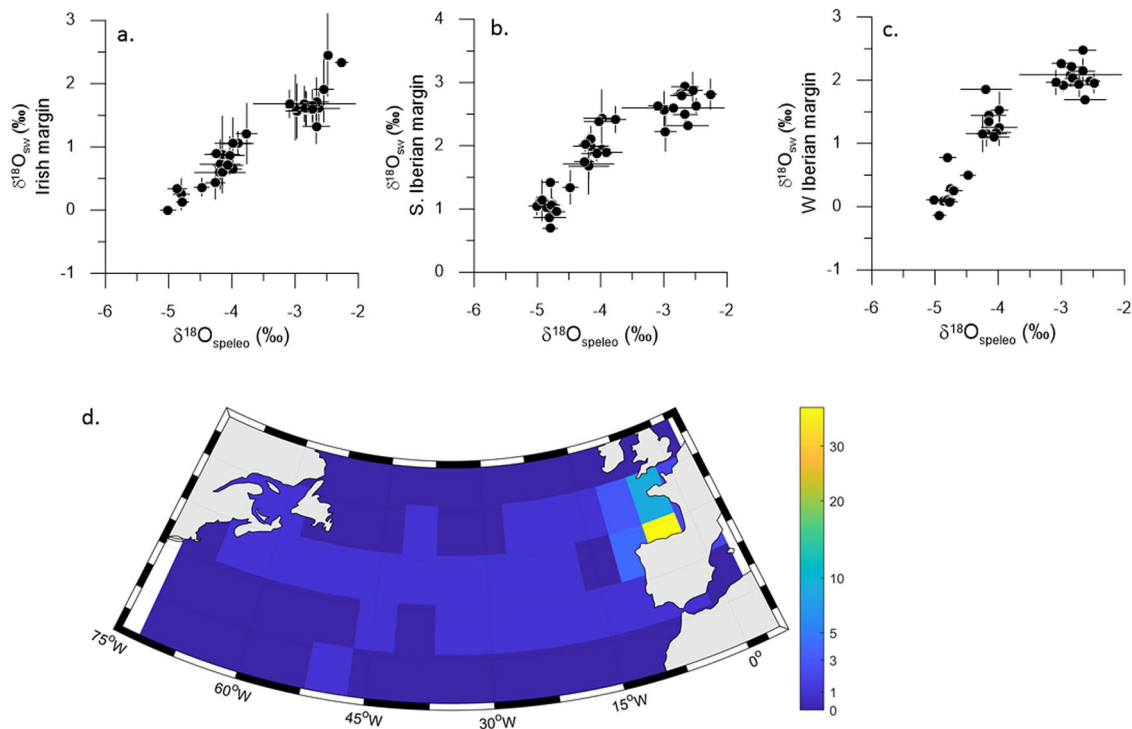


Fig. 2 Prediction of $\delta^{18}\text{O}_{\text{sw}}$ from $\delta^{18}\text{O}_{\text{NISA}}$. **a–c** $\delta^{18}\text{O}_{\text{sw}}$ vs $\delta^{18}\text{O}_{\text{NISA}}$ in fixed 500 ky bins over the time interval from 25 to 5 ka BP, on original marine chronologies. Horizontal and vertical lines illustrate plus and minus one standard deviation of the $\delta^{18}\text{O}$ data to illustrate the range of variation within each age bin. Results show $\delta^{18}\text{O}_{\text{sw}}$ from the a) Irish margin^{16,32}, $r^2 = 0.91$. **b** W. Iberian margin¹⁸, $r^2 = 0.85$. **c** S. Iberian margin¹⁷, $r^2 = 0.85$. **d** Proportion (as %) of oceanic moisture recharge events originating in each $5^\circ \times 5^\circ$ grid over the ocean, for precipitation events 2015–2016 near the cave location, as described in Methods. For regressions, all p -values are < 0.001 ; full data in Supplementary Table 1.

maintained in the eastern North Atlantic for a duration of ~ 600 yrs before the rate of warming increased and over several centuries the surface ocean $\delta^{18}\text{O}$ anomaly was reduced (Fig. 4b). We infer that slowed meltwater flux and re-invigorated AMOC dissipated the $\delta^{18}\text{O}$ anomaly through dilution and mixing of meltwater throughout the global ocean.

Following the second and most intense negative $\delta^{18}\text{O}$ shift (MWPTII-B) and AMOC slowdown, a North Atlantic freshwater $\delta^{18}\text{O}$ anomaly persisted. Unusually, for ~ 3000 years, the $\delta^{18}\text{O}_{\text{NISA}}$ remained lower than the final interglacial state. The maintenance of a freshwater $\delta^{18}\text{O}$ anomaly for so long in the surface eastern North Atlantic requires addition of meltwater at rates greater than it can be distributed through mixing with the global ocean. Thereafter, starting around 131 ka, the North Atlantic freshwater $\delta^{18}\text{O}$ anomaly diminishes rapidly, which suggests that the rate of addition of meltwater into the eastern North Atlantic had slowed sufficiently so that ocean circulation homogenized the deglacial meltwater anomaly to the global ocean average. This decline coincides with a rapid decrease in IRD delivery in the Northeast Atlantic and Labrador Sea (Fig. 4b, Supplementary Fig. 12). The rate of decrease in $\delta^{18}\text{O}$ of benthic foraminifera ($\delta^{18}\text{O}_{\text{benthic}}$) on the Iberian margin also slowed significantly at 131 ka (Figs. 4 and 5), consistent with slowed melt rate.

We detect late phases of melting between 130 and 129 ka. A rapid negative shift in $\delta^{18}\text{O}_{\text{NISA}}$ around 129.7 ka, during regional warming, likely reflects acceleration of meltwater addition. Notably, the continued meltwater flux through 129.3 ka appears to coincide with the deposition of a distinctive sediment layer on the Labrador margin³³ which occurred at ~ 129.3 ka on our chronology (Supplementary Fig. 13), a depositional event attributed to a final North American Ice Sheet (NAIS) flood outburst, analogous to the 8.2 ka event following TI. The 8.2 ka event initiated when $\sim 90\%$ of North American ice had melted³⁴, so if the sediment layer at

129.3 ka is analogous³³, it suggests that a similarly high fraction of melting of PGM NAIS ice was likewise complete by this time.

On the W Iberian margin, our speleothem based chronology for TII indicates a much faster rate of depletion in $\delta^{18}\text{O}_{\text{benthic}}$ during TII than during TI, suggesting that deep waters in the North Atlantic underwent freshening much more rapidly in TII than during TI (Fig. 5). The chronology of the global marine $\delta^{18}\text{O}_{\text{benthic}}$ stack³⁵, used as index of glacial ice volume to estimate rates of deglaciation and as inputs for model calculations³⁶ is based on tuning to NH summer insolation, assuming a comparable phase relationship to TI. $\delta^{18}\text{O}_{\text{benthic}}$ curves have also previously been used to estimate sea level³⁷ and the rate of sea level rise⁹ during TII compared to TI. However, our chronology suggests that the rapid TII deglaciation precedes the peak in high latitude NH summer insolation and the existing chronology³⁵ probably yields minimum estimates of rates of deglaciation. The speleothem chronology for the $\delta^{18}\text{O}_{\text{benthic}}$ on the W Iberian margin provides an alternate estimate of the rate of sea level change and deglaciation (Fig. 5). This likely represents the upper estimate of the rate of sea level rise, duration, and amplitude of freshwater forcing compared to those employed in recent models using original chronology⁹. Our independent tuned chronology for $\delta^{18}\text{O}_{\text{benthic}}$ -based sea level estimates are closest to the oldest chronology (95% upper CI) for the Red Sea curve^{38,39}, and our chronology implies the potential for an earlier and even more concentrated meltwater pulse than estimated from the derivative of the Red Sea sea level curve (Fig. 5)⁴⁰.

Similarities and contrasts between the meltwater anomaly during TI and TII deglaciation. Our speleothem absolute chronology confirms that both TI and TII deglaciations initiated at a similar threshold of caloric summer insolation (5.8 GJ m^{-2})

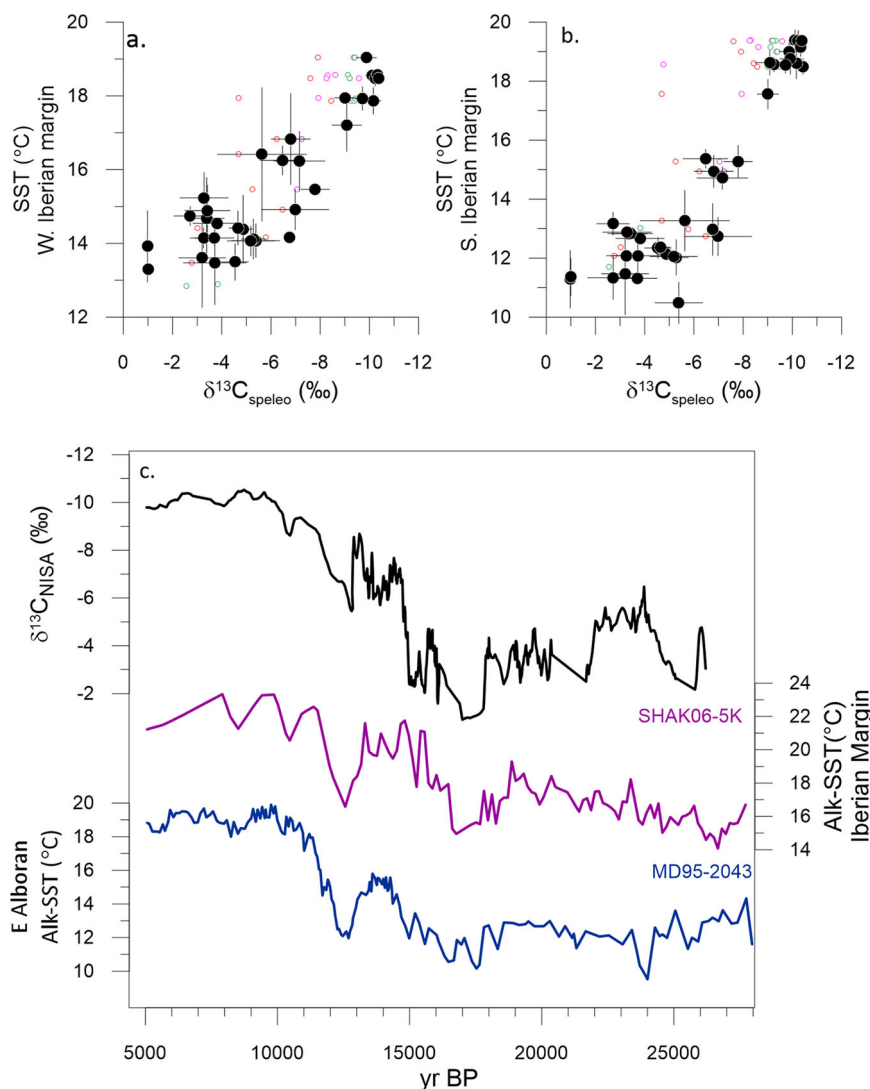


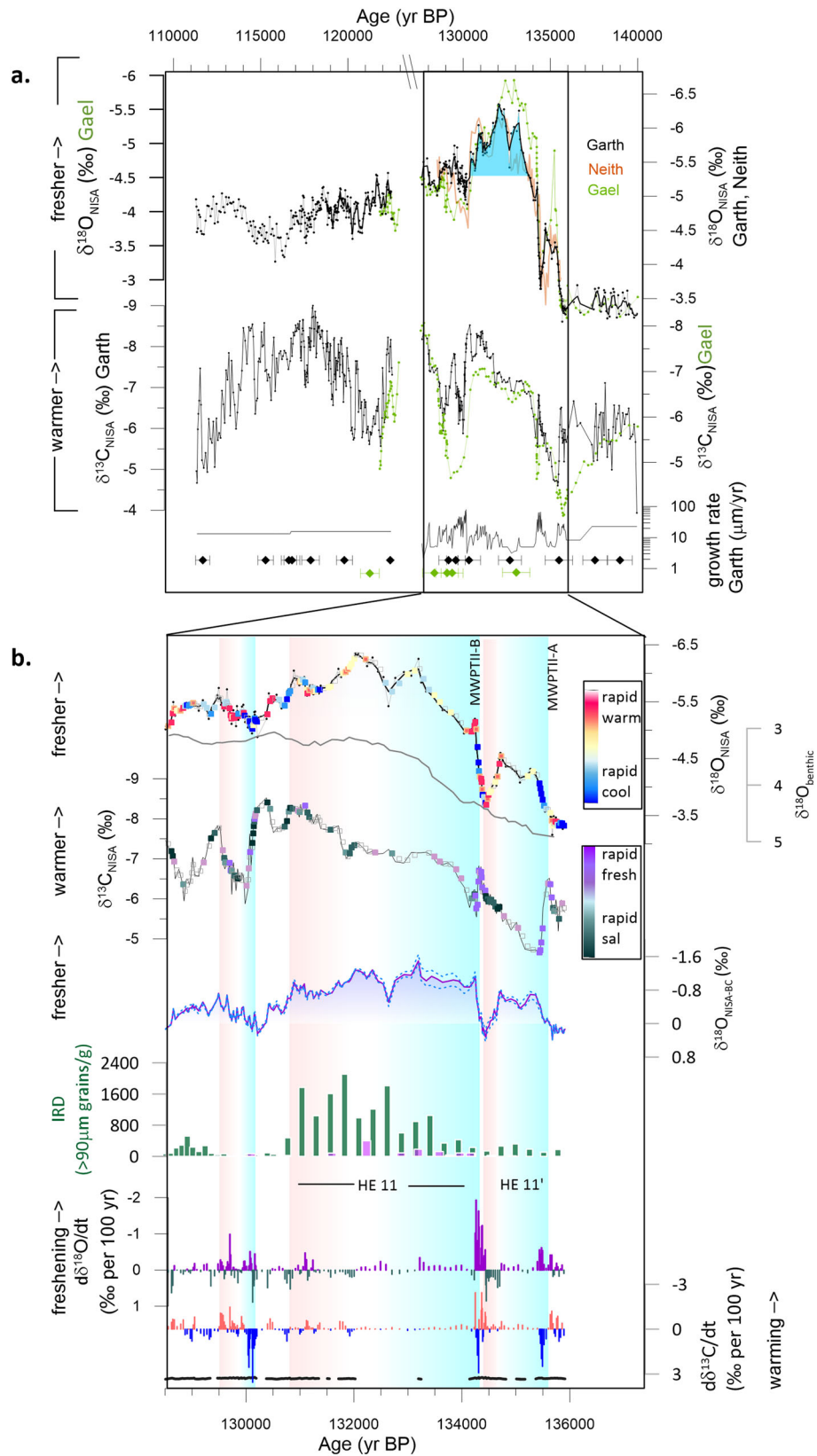
Fig. 3 Relationship between regional temperature and NW Iberian speleothem $\delta^{13}\text{C}_{\text{NISA}}$ over TI. **a, b** The scatterplots show $\delta^{13}\text{C}_{\text{NISA}}$ for fixed time bins (500 years) from stalagmites Candela, Galia, Laura, and Alicia, vs alkenone SST from the S Iberian margin⁹⁵ and W Iberian Margin²⁹ respectively. Black symbols denote the average for the splice, and small colored symbols denote stalagmite increments where they do not comprise the splice, from Candela (red), Laura (brown), Galia (green) and Alicia (fuchsia). For the S. Iberian margin, $r^2 = 0.87$ and $p \ll 0.01$. For the W. Iberian margin, $r^2 = 0.82$ and $p \ll 0.01$. **c** Time series of the NISA $\delta^{13}\text{C}_{\text{NISA}}$ splice, and the alkenone SST from the MD95-2043 on S Iberian margin⁹⁵ and SHAK06-5K on W Iberian Margin²⁹.

(Fig. 6). Yet, the speleothem chronology for $\delta^{18}\text{O}_{\text{benthic}}$ reveals attainment of interglacial values within ~ 5 ky of the TII deglacial onset, compared to nearly 9 ky in the TI deglaciation. Notably, the development of the eastern North Atlantic $\delta^{18}\text{O}_{\text{sw}}$ anomaly during TII is markedly different from that of TI (Fig. 6). During TII, $\delta^{18}\text{O}_{\text{sw}}$ remained more negative than the final interglacial state for nearly 3000 years, a situation which never occurred in TI. During TI, the regional surface ocean $\delta^{18}\text{O}_{\text{sw}}$ anomaly, calculated relative to the benthic $\delta^{18}\text{O}_{\text{calcite}}$ on the Iberian margin ($(\delta^{18}\text{O}_{\text{NISA-BC}}$; Methods), remains below -1‰ only between 16.4 and 15.2 ka (1.2 ky duration), whereas during TII it remains below -1‰ from 134.7 to 131.2 (3.5 ky duration; Fig. 6).

During TI, this period of greatest regional $\delta^{18}\text{O}_{\text{sw}}$ anomaly coincides with the interval of fast melt rate of the Eurasian ice sheet according to recent sea level reconstructions⁴¹ (Fig. 7; Supplementary Fig. 16). One interpretation is that EIS meltwater leads to a greater negative $\delta^{18}\text{O}_{\text{sw}}$ anomaly in the eastern north Atlantic compared to NAIS meltwater. Southward advection of surface waters from the Nordic seas along the European continental margin is simulated during periods of retreat of the

northern and western EIS²⁰. Intermediate complexity models comparing identical freshwater forcing in different outlets infer a greater salinity anomaly in the eastern North Atlantic due to Eurasian meltwater compared to North American meltwater routed through Hudson Bay, Gulf of Mexico, or Gulf of St. Lawrence. This is because for these NAIS routes, the salinity (and $\delta^{18}\text{O}_{\text{sw}}$ anomaly) would be diluted during advection across the Atlantic by the North Atlantic Drift⁴². These model simulations, albeit limited, suggest the potential for higher amplitude $\delta^{18}\text{O}_{\text{sw}}$ anomaly in the eastern North Atlantic during EIS melt than NAIS melt, given similar $\delta^{18}\text{O}_{\text{ice}}$ as assumed in previous studies⁴³. Therefore, one explanation for the longer duration surface ocean $\delta^{18}\text{O}_{\text{sw}}$ anomaly during TII is a larger proportion of EIS-derived meltwater in TII compared to TI.

In support of this explanation, Eurasian PGM deposits are found well beyond the limit of ice extent from the LGM, with the largest expansion in the Barents-Kara sectors of northern Russia (Fig. 1). However, the sparse direct chronology of ice positions does not distinguish if these advances were synchronous across all sectors to yield at a single time during the penultimate glacial a



significantly larger EIS, or if, as in the last glacial cycle, sectors were out of phase^{44,45}. The potential for a larger PGM EIS ice sheet has been explored in dynamical ice sheet models with total EIS ice volumes of up to 70 m sea-level equivalent, nearly triple that of the LGM EIS⁴⁶. Because of similar estimated PGM and

LGM sea level and benthic $\delta^{18}\text{O}$, this simulated large PGM EIS likely coexisted with a smaller than LGM NAIS⁴⁶. The ice sheet reconstruction featuring a large TII EIS⁴⁶ encompasses a 2.5–3.5x greater volume of marine-grounded (grounded below paleo sea level) EIS ice at the PGM, compared to the LGM (Methods) with

Fig. 4 New NW Iberian speleothem records spanning TII. **a** Measured isotope records from stalagmites Garth (black), Neith (orange) and Gael (green), together with speleothem growth rate in Garth, and position of ^{230}Th dates in Garth and Gael and their analytical error. A scale break is used for strongly condensed growth between 128 and 122 ka; full records in this time are shown in Supplementary Fig. 13 and 14. Blue infill in Garth record highlights when $\delta^{18}\text{O}_{\text{NISA}}$ is $>0.5\%$ more depleted than at interglacial onset. **b** Detail of the deglacial period records from Garth, together with $\delta^{18}\text{O}_{\text{benthic}}$ from MD01-2444⁵⁹ on speleothem age model as described in Supplement, and $\delta^{18}\text{O}_{\text{NISA-BC}}$ (purple line with shading), the $\delta^{18}\text{O}_{\text{NISA}}$ minus the benthic component of $\delta^{18}\text{O}$ change, calculated as detailed in Methods, and the IRD abundance at ODP 983¹⁰⁹ and MD01-2444¹⁸. The $\delta^{18}\text{O}_{\text{NISA}}$ is color coded according to the rate of warming or cooling inferred from the rate of change in $\delta^{13}\text{C}_{\text{NISA}}$ to highlight the temperature forcing and feedbacks on North Atlantic $\delta^{18}\text{O}$. Likewise, the $\delta^{13}\text{C}_{\text{NISA}}$ is color coded according to the rate of freshening inferred from the rate of change in $\delta^{18}\text{O}_{\text{NISA}}$. Rate of change in $\delta^{18}\text{O}_{\text{NISA}}$ and $\delta^{13}\text{C}_{\text{NISA}}$ ($\%_{\text{cc}}$) per 100 year, uses the smoothed isotope records from speleothem Garth shown. Bottom line indicates periods during which seasonally resolved fluorescent layers are present and used to define speleothem growth rate. Consistent with definition of HE by IRD, we designate the period initiating with MWP-TIIB as HE11, and denote the earlier phase of meltwater and AMOC reduction HE11'.

thickest ice in the Fennoscandian sector. Because of isostatic loading and higher relative sea level caused by self-gravitation, the larger PGM EIS would have been even more sensitive to ocean forcing and marine ice sheet instability which could have contributed to a rapid retreat. Although the onset of modeled TII EIS retreat differs slightly from our record⁸, its duration is broadly consistent with the here documented duration of eastern North Atlantic $\delta^{18}\text{O}$ anomaly.

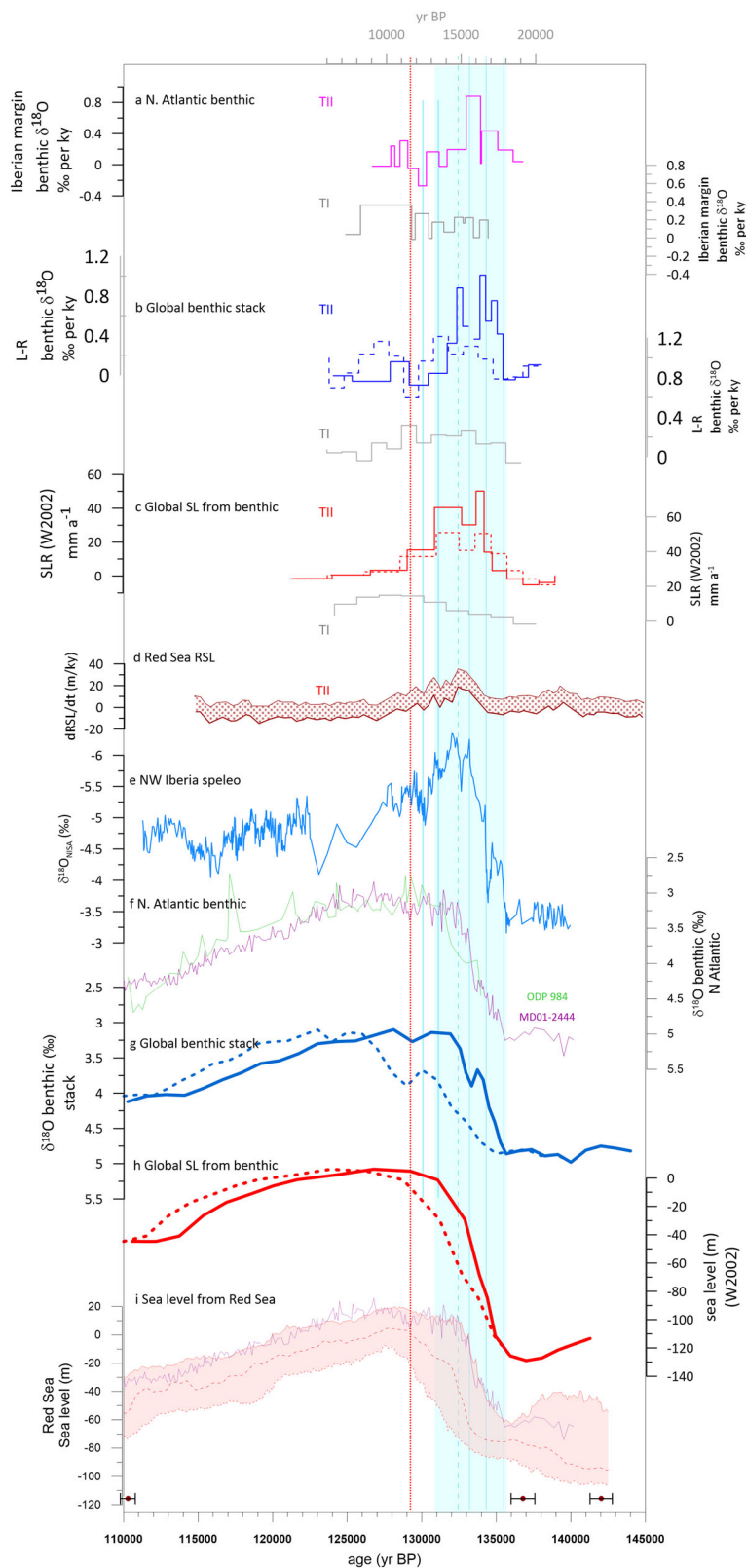
An alternative explanation for the greater freshening in the eastern N Atlantic during TII is that LGM-like ice sheet configuration melted faster in TII than in TI. However, we consider this scenario less likely because it would require faster melting of the portions of NAIS which were longest lived during TI, and we have no evidence of a stronger forcing during TII. An Arctic ice shelf, neutrally buoyant but potentially containing a freshwater equivalent to 10 m s.l.e. is proposed to have existed at some time during the penultimate glacial cycle but the timing of formation and collapse remains controversial^{47–49}. Based on our records, we cannot confirm nor rule out disintegration of such an ice shelf as a contributor to freshening at the onset of TII, leading the retreat of Northern sectors of the EIS. However, the modest magnitude of Arctic shelf ice volume suggests that this cannot be the only factor responsible for differences in the meltwater anomaly and rate of change in $\delta^{18}\text{O}_{\text{benthic}}$ and sea level rise over TII (Figs. 5 and 6).

In addition, models suggest that the intensity and duration of the regional $\delta^{18}\text{O}_{\text{sw}}$ meltwater anomaly are also increased by a slowing of the rate of dilution of the meltwater signal, primarily because slowed overturning circulation reduces the vertical dissipation rate¹¹. During TI, the greatest regional freshening anomaly (16.4 to 15.2 ka) also coincides with a period of AMOC reduction inferred from proxies such as Pa/Th⁵⁰ (Fig. 7, Supplementary Fig. 16). For this time interval, the relative importance of the EIS meltwater source vs AMOC amplification of meltwater anomaly cannot yet be directly deconvolved because existing Pa/Th records suggest only a 30% AMOC reduction during HE1⁵¹ while the high resolution isotope-enabled OA-GCM experiments simulate a very extreme AMOC shutdown (from 16 to 2.5 Sv). Nonetheless, the temporal coincidence of reduced AMOC and the phase of most rapid EIS retreat in TI may not be coincidence. Simulations suggest that meltwater release from the Northern and western margin of the EIS (and the Mackenzie River outlet of the North Americans), is more effective at decreasing AMOC compared to North American melt routed through the Gulf of Mexico, Hudson Bay, or St. Lawrence outflows^{42,52}, because the former meltwaters reach the locations of northern North Atlantic convection with lesser dilution by other surface waters⁵³. Therefore, the strong surface meltwater $\delta^{18}\text{O}_{\text{sw}}$ between 16.4 and 15.2 ka in the eastern north Atlantic may be both a direct consequence of high EIS melt rates releasing water in the eastern North Atlantic, and an indirect consequence of the high EIS melt rates on AMOC stability and concomitant

amplification of the surface meltwater $\delta^{18}\text{O}_{\text{sw}}$. In and of itself, reduced AMOC intensity, such as that inferred to have occurred during the Younger Dryas according to Pa/Th (Fig. 7, Supplementary Fig. 16), does not coincide with a large freshwater $\delta^{18}\text{O}_{\text{sw}}$ anomaly in the eastern North Atlantic. This suggests that the EIS source effect may be the dominant factor leading to the surface meltwater $\delta^{18}\text{O}_{\text{sw}}$ anomaly early in TI. This hypothesis should be further explored in experiments in high resolution coupled OA-GCM simulations with meltwater release in realistic regions, also exploring the effect of a range of AMOC reduction intensities on the rate of dissipation and therefore the amplitude and persistence of meltwater $\delta^{18}\text{O}_{\text{sw}}$ anomaly.

Further evidence for continual meltwater flux during the long TII meltwater anomaly comes from marine IRD records. On our speleothem chronology, marine records show that peak IRD deposition in both the northeastern Atlantic ODP sites 983 and 984 as well as in sites around the Iberian Margin coincides with the long $\delta^{18}\text{O}_{\text{NISA}}$ anomaly. Because large IRD fluxes are commonly interpreted to reflect a high flux of ice calving from instability in marine-terminating ice sheets⁵⁴, the IRD peak suggests that the long surface ocean $\delta^{18}\text{O}$ anomaly was not the result of slowed ocean circulation alone, but that continued meltwater addition from decaying ice sheets either contributed to or was the dominant driver of the signal (Fig. 4b). Large North Atlantic IRD and Heinrich Events (HE) have been linked to the large meltwater release during multiple glacial terminations⁵⁵. We suggest this period corresponds to HE11, and distinguish the first freshening-induced AMOC slowdown of MWPTII-A as HE11'. While the amplitude and duration of the eastern North Atlantic $\delta^{18}\text{O}$ anomaly may potentially be enhanced if the release of meltwater shuts down AMOC¹¹, we consider it unlikely that a more intense or longer duration of AMOC weakening during TII is the only cause for the long period of extreme eastern North Atlantic $\delta^{18}\text{O}$ fresh anomaly. Although there are no direct quantitative proxies for AMOC intensity in TI or TII⁵¹, some mid-latitude proxy records are likely to be sensitive to the strong winter season climatic impacts of AMOC slowdown such as the relative abundance of *Neogloboquadrina pachyderma sinistral*⁵⁶ or relative abundance of $\text{C}_{37:4}$ alkenone^{57–59} (Fig. 6). These climatic indicators suggest a less extreme AMOC slowdown and sea ice response to stratification during HE11 in TII than in HE1 during TI (Fig. 6, Supplementary Fig. 9). The duration of HE11 and HE1 are comparable. Thus, available evidence would not support a difference in physical circulation as the only cause for the contrasting surface ocean eastern North Atlantic $\delta^{18}\text{O}$ anomaly in TI vs TII.

Based on these considerations, we suggest that our record of freshening is most consistent with a PGM EIS much larger than its LGM counterpart, and is compatible with the larger EIS volume scenarios of 60 m to 71 m sea level equivalent^{60,61} based on glacial-isostatic modelling. Further ice sheet modeling and assimilation of near field geophysical data are required to evaluate this interpretation.



Causes and feedbacks from meltwater-induced AMOC disruption. Our new, highly resolved record of TII reveals that, as in TI, the deglacial sequence was characterized by a series of millennial-scale variations not previously resolved in records of sea level rise^{35,37–40}. We find evidence for multiple phases of AMOC reduction and reinvasion in TII which provide new

clues to the mechanisms of AMOC instability during glacial terminations. It has been debated, whether meltwater release causes AMOC reduction, or if it is the subsurface ocean warming during AMOC shutdown that causes accelerated ice sheet collapse and meltwater release⁵³. Here, our new annually laminated records show that enhanced freshwater addition during brief

Fig. 5 Rates of change in $\delta^{18}\text{O}_{\text{benthic}}$ and sea level during TII. **a–d** Compare rates of change in $\delta^{18}\text{O}_{\text{benthic}}$ and sea level records during TI and TII. The respective benthic $\delta^{18}\text{O}_{\text{benthic}}$ and sea level curves spanning TII are illustrated in panels **f–i**. The NW Iberia $\delta^{18}\text{O}_{\text{NISA}}$ from Garth is shown in **e**. Sources are: W Iberian margin $\delta^{18}\text{O}_{\text{benthic}}$ records in TI^{18,59} following tuning to NW Iberian speleothem chronology (purple); comparison with rate of change in W Iberian margin $\delta^{18}\text{O}_{\text{benthic}}$ records in TI^{94,110}. Global $\delta^{18}\text{O}_{\text{benthic}}$ stack³⁵ for TII on original chronology (dashed red line) and our proposed maximum rate chronology (solid red line). Waelbroeck 2002 sea level curve from $\delta^{18}\text{O}_{\text{benthic}}$ stack³⁷ for TII on original chronology (dashed blue line) and our proposed maximum rate chronology (solid blue line). The Red Sea sea level record and its 95% CI is shown with red shading on its published chronology the 95% confidence interval estimated on the rate of sea level change is shown as reported⁴⁰. At the base of the figure are shown the three age control tie points tuning the Red Sea record to a Mediterranean $\delta^{18}\text{O}_{\text{planktic}}$ record (LC41) and their uncertainties³⁸. These anchor the age model used to calculate the rate of freshwater addition from the derivative of the sea level curve. The uncertainties in the original Red Sea chronology do not preclude the rates of sea-level change we estimate through application of speleothem chronology to $\delta^{18}\text{O}_{\text{benthic}}$. Blue vertical bar highlights HE11 as in Fig. 3, and the timing of NAIS outburst event is shown with red line. **i** The W. Iberian margin $\delta^{18}\text{O}_{\text{benthic}}$ is shown overlain on the Red Sea sea level curve to facilitate comparison of these two independent chronologies.

periods of rapid warming led, and therefore likely caused, AMOC reductions early in TII.

AMOC recovery has most often been attributed to a slowing of the rate of meltwater addition. Alternatively, recent model experiments suggest that AMOC can also recover, despite sustained meltwater flux, if there is a change in the boundary conditions which set the threshold for weakened AMOC. For example, AMOC may have recovered after HE1 in TI during the Bølling-Allerød because the rapid CO_2 rise during HE1 raised the forcing threshold required to maintain weak AMOC^{5,62}. TII was previously proposed to lack such a mid-termination AMOC recovery⁵. Yet, we identify a recovery after the first AMOC reduction of TII (Fig. 4b). This event occurred earlier in the deglaciation (e.g. $\delta^{18}\text{O}_{\text{benthic}}$ on the Iberian margin was 4.45 ‰ during the TII recovery compared to 4.25‰ at the start of the Bølling-Allerød) (Fig. 6). One possibility is that AMOC recoveries at TII may have been driven not by evolving thresholds in AMOC sensitivity but rather by strong temporal variations in meltwater forcing. This short duration of the first TII AMOC reduction (600 years vs ~3000 years for HE1 in TI) may reflect the operation of a negative feedback of AMOC slowdown on TII melting rate, if the main location of early TII melting occurred in an area sensitive to AMOC-induced cooling.

On the other hand, if a change in boundary conditions is required for AMOC recovery, then our results in TII present a paradox, because according to the current available ice core chronology, the onset of the first AMOC recovery occurred when CO_2 had risen only to 207 ppmv⁷, much less than the 245 ppmv attained by the onset of the Bølling-Allerød (Fig. 8)⁷. Even by the end of HE11, according to AICC2012 chronology, pCO_2 had only reached 245 ppmv, much less than the 260 ppm reached by the end of the Younger Dryas. This ice core CO_2 chronology would suggest a very different sensitivity of AMOC to CO_2 between TI and TII. This circumstance could reflect other initial boundary conditions, such as a lower glacial height of the North American ice sheet or different initial PGM thermohaline regime⁶³, which conditioned the AMOC threshold.

It is also possible that ice core records may underestimate the rate of TII CO_2 rise due to the differing precision of age models based on annual layer counting for TII⁶⁴, and age models based on age interpolation between two age control points at 121 and 135 ka tuning ice core O_2/N_2 ratios to local summer insolation⁶⁵. The chronology of the main TII CO_2 rise can be further explored from an available marine CO_2 proxy record based on planktic foraminifera $\delta^{11}\text{B}$ from the western Caribbean⁶⁶. This record indicates a large initial CO_2 rise synchronous with a surface ocean freshening recorded by the same planktic foraminifera⁶⁷. Although tuning this site to our speleothem chronology has some uncertainty (Methods, Supplementary Fig. 17), and proxy CO_2 estimates are less precise than direct measurements in ice

cores, a conservative correlation suggests that a larger portion of the deglacial CO_2 rise may have occurred rapidly, coincident with the onset of rapid EIS melting and the second AMOC slowdown (Fig. 7). An early and rapid CO_2 rise, introducing greenhouse-forced warming, is also consistent with the progressive warming above glacial background levels occurring after MWP-TIIB in our air temperature record, which would have maintained the melting of NH ice sheets during the HE11 AMOC slowdown (Fig. 8). Thus, diagnosing the links between rate of ice melting, AMOC recovery, and deep ocean carbon storage during TII may require reassessment of the rate of CO_2 rise.

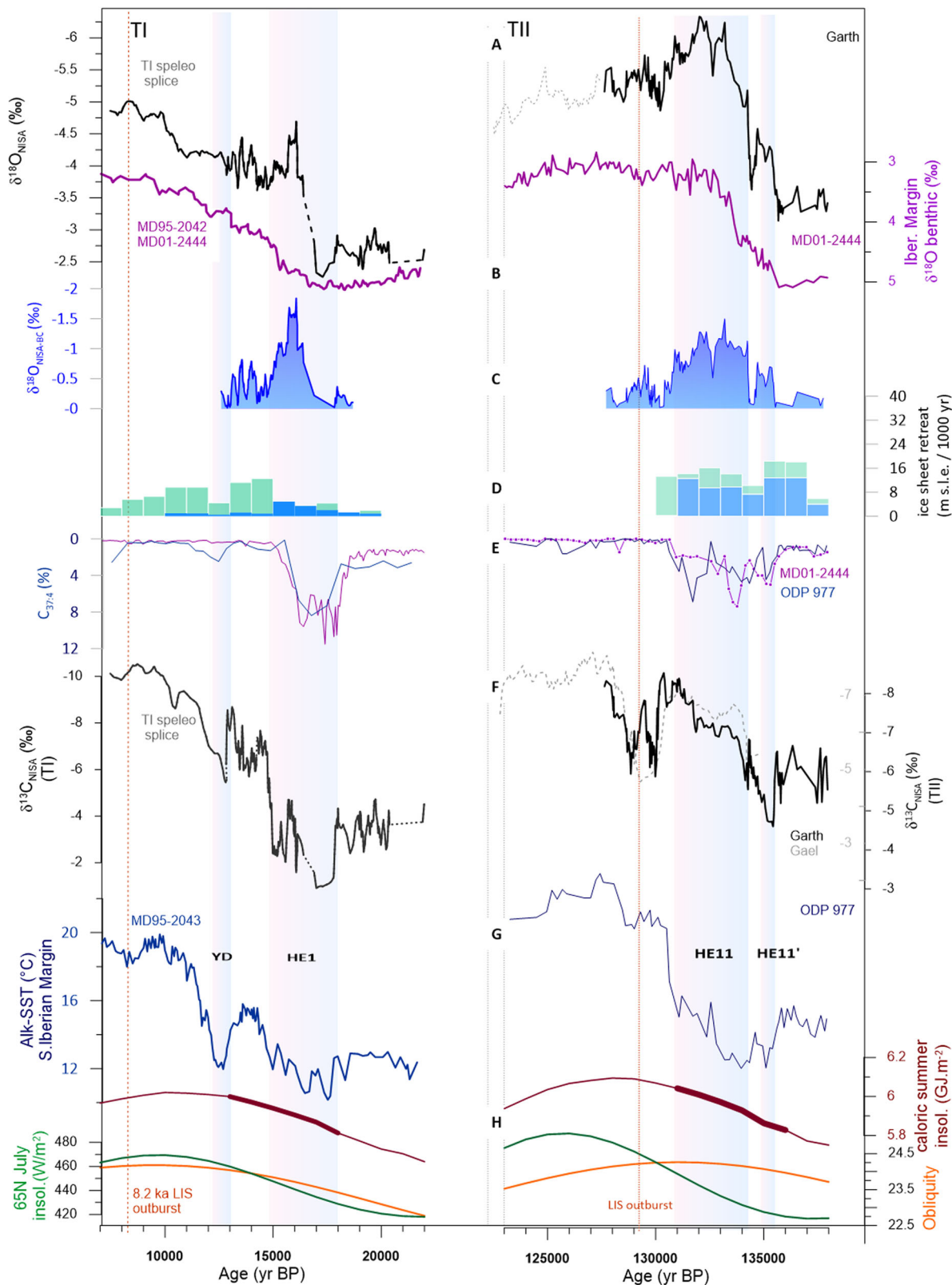
Overall, the first direct absolute age constraints on the timing and rate of TII freshwater release to the North Atlantic are consistent with a large EIS, which was prone to rapid retreat due to its enlarged marine-based boundaries. These observations highlight the control that glacial boundary conditions exert, by shaping ice sheet anatomy, over the rates of ice melting and also the nature of the subsequent interglacial^{9,68}. The new records also provide the first evidence for discrete centennial scale meltwater pulses indicative of phases of accelerated ice sheet failure during TII and a detailed view of their coupling with cooling consistent with AMOC reductions. The role of internal ice processes and climate feedbacks associated with the retreat of large marine-based northern hemisphere ice sheets should be further investigated with coupled ocean-climate-ice sheet models.

Methods

Identification of final moisture source exchange via backtracking. Moisture uptake regions of 104 rain events which were sampled <100 km west of the cave during 2015 and 2016, were calculated using backward-trajectory analysis with 1 h temporal resolution, performed using the Hybrid Single-Particle Lagrangian Integrated Trajectory (HYSPLIT) Model (Version 4.8)⁶⁹ and following a similar methodology as previous studies⁷⁰. Moisture uptake regions along 850 hPa, 700 hPa and 500 hPa were identified using a specific humidity threshold of 0.5 g/kg increment in at least 6 h, using meteorological data provided by backward-trajectories. Results are shown in Fig. 2d.

Stalagmite samples. Stalagmite samples were analyzed from the following previously described⁷¹ NW Iberian caves: Pindal Cave (stalagmites Candela, Laura), La Vallina Cave (Garth, Gael, Galia, Gloria), and Cueva Rosa (Neith, Alicia). These stalagmites cover TI, Greenland Stadial 22 (GS22), and TII^{27,71,72}. Additional growth phases have been studied in the stalagmite Candela since earlier publication⁷², and we report additional dates and higher resolution geochemical data. In Candela, A ~10 cm long basal growth phase (CANB) has been sampled along its main growth axis and redated, contrasting with strongly off-axis and condensed sampling of this phase in earlier work. Additionally, within the Bølling-Allerød, a transient 1.5 cm shift in growth axis has been resampled along its expanded central growth axis for 2.5 cm, expanding by 5-fold the record previously sampled in a lateral portion at only 0.5 cm thickness.

Measurement of seasonal fluorescent banding for growth rate evaluation in key intervals. To account for variation in growth rates⁷³ between ^{230}Th dates, for intervals of rapid freshening in TI and TII, we refine age models by estimating stalagmite growth rates from the width of growth bands defined by fluorescent



layers⁷⁴ which have been described to result from seasonal delivery and/or incorporation of fluorescent organic substances in dripwater⁷⁵.

Stalagmite slabs were mounted in low-viscosity Laromin C260 epoxy (cycloaliphatic diamine polymer), ground flat with SiC paper, and then polished with a diamond suspension to 0.25 μm in preparation for Confocal laser scanning microscopy (CLSM) and laser ablation ICP-MS. Imaging by CLSM was performed at the Scientific Center for Optical and Electron Microscopy (ScopeM) at ETH Höggerberg using an Olympus Fluoview 3000. Here, a series of overlapping

images were obtained under 100–200x magnification using an incident wavelength of 488 nm and measuring fluorescence in a 490–590 nm window. Images were obtained at 1024 × 1024 or 2048 × 2048 resolution, corresponding to 1.2 to 0.6 μm/pixel (respectively) under 100x magnification. Images were processed using Fiji/ImageJ, where the exact distances between growth layers were recorded on an absolute length scale and later cross-referenced to laser ablation and drilling (isotope, trace element) data. Confocal images were counted in stalagmite Garth section from 177.5 to 269.5 mm from the tip. Growth layer thickness was used to

Fig. 6 Comparison of deglacial evolution in North Atlantic during TI and TII. Synthesis of speleothem records from NW Iberia over TI (left panel) and TII (right panel) and marine records tuned to NW Iberian speleothem chronology. **A** Black line shows $\delta^{18}\text{O}_{\text{NISA}}$ record from speleothem Garth (black line) and Gael (dashed line) for TII and TI speleo splice (see Supplementary Figs. 2 and 13). **B** Iberian Margin $\delta^{18}\text{O}_{\text{benthic}}$. **C** Eastern North Atlantic meltwater $\delta^{18}\text{O}$ anomaly estimated from $\delta^{18}\text{O}_{\text{NISA-BC}}$ calculated as described in Methods **(D)** rate of NH ice sheet melting in 1 ky age bins, for TI from^{34,41} and TII⁸. **E** $\text{C}_{37:4}$ abundance on the W. and S. Iberian margin^{58,59} indicator of sea ice proximity **(F)** $\delta^{13}\text{C}_{\text{NISA}}$ from Garth and TI splice, as temperature indicator **(G)** alkenone SST in the S. Iberian Margin^{92,95}. **H** Variation in orbital parameters: caloric summer at 55°N (brown) obliquity (orange), and 65°N July insolation (green), with bold color highlighting caloric summer interval when eastern North Atlantic freshens faster than the global average. Vertical dashed red line indicates the NAIS outburst flood at end of TII³³ and the 8.2 ka outburst linked to final NAIS collapse¹¹¹.

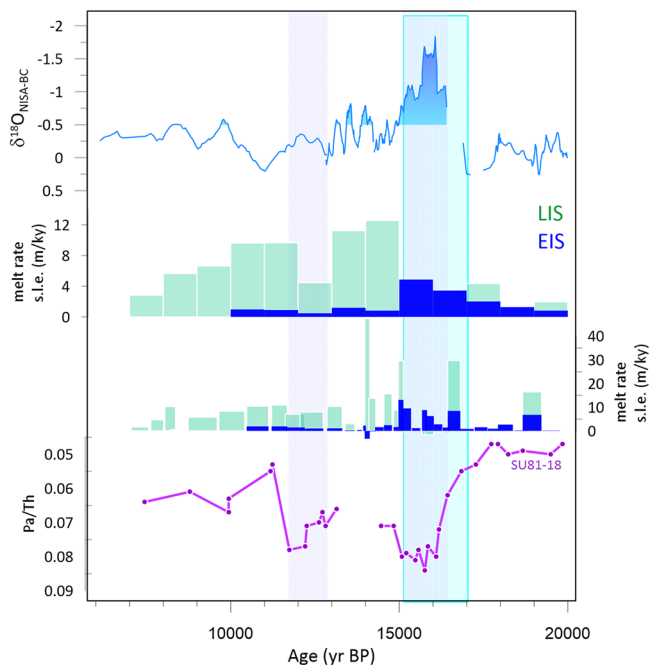


Fig. 7 Time series of regional $\delta^{18}\text{O}_{\text{sw}}$ anomaly over TI vs NH melting rate and AMOC indicators. Regional freshwater anomaly $\delta^{18}\text{O}_{\text{NISA-BC}}$ compared with estimations of the melting rate NAIS and EIS, from⁴¹ (20 to 12 ka) and from³⁴ (6–12 ka). Shown are melt rates derived from sea level curves interpolated to uniform 1 ky resolution, to facilitate comparison to TII available only at this resolution (Fig. 3), as well as rates at original published resolution. Also shown is the Pa/Th indicator of AMOC intensity⁵⁰.

determine rates of isotopic change in sections which could be layer counted, and to develop accurate interpolation of ages between U/Th dates. In areas where annual layers were not immediately visible, typically when layer thickness was less than 3 μm , an average growth rate for that section was assigned in order to be consistent with the sequence of U/Th ages.

^{230}Th and ^{14}C absolute dating and age model development. Absolute chronology is based on subsamples drilled for ^{230}Th dating. New dating was completed using standard methods and analysis on MC-ICP-MS (Thermo-Finnigan Neptune)⁷⁶ at Xi'an Jiaotong University and the University of Minnesota; some previously published aged used in this study also include determinations on SF-ICP-MS (Thermo-Finnigan ELEMENT⁷⁷); results are given in Supplement Tables 4 and 6. To evaluate growth rate in stalagmite Laura, ^{14}C ages were measured at ETH Zurich with a gas ion source in a Mini Carbon Dating System at the Laboratory of Ion Beam Physics, ETH, via on-line acid digestion⁷⁸ and calibrated with INTCAL 2020⁷⁹ and results are given in Supplement Table 5. No new age models are elaborated for GS22 and these are shown in²⁷. Because agricultural and pasture land uses became widespread in Northern Spain after 5.5 ka BP⁸⁰ which may decouple the natural relationships between climate and vegetation over cave sites, we do not present or discuss speleothem records younger than 5 ka BP.

Age models for stalagmites younger than 30 ky are illustrated in Supplementary Fig. 1. Sequences of multiple ^{230}Th ages are interpolated using the Bchron software^{81,82} (Maria, Candela, Galia, and Alicia A) whereas linear interpolation was employed for short growth phases bracketed only by basal and top U/Th dates (Alicia B, C). Two approaches are used to refine the age model within the 18 to 14 ka interval in Candela. Where visible growth laminae are present, their thickness

is used to constrain growth rates (green line in growth rate curve in Supplementary Fig. 1a) and to identify the point at which growth becomes most strongly condensed. For example, the age model is pinned at a new MC age at $18.0 \text{ ka} \pm 78 \text{ year}$ ^{230}Th date (at reference level 4.5 mm), and advanced upwards $\sim 90 \text{ year}$ using width of fluorescent growth layers to constrain growth rate. Growth layers are not countable in the following 7.7 mm of stalagmite (brown line in Supplementary Fig. 1a). Consequently, in this section two tie points with the geochemical variations in stalagmite Laura (red points in Supplementary Fig. 1a) were used to constrain the Candela age model, and growth rate was varied from 10 to $1 \mu\text{m}/\text{year}$ inversely with Candela $\delta^{13}\text{C}$, with a 630 year negligible deposition ($< 0.2 \mu\text{m}/\text{year}$) interval at the end of the $\delta^{13}\text{C}$ maximum. The precision of the age model is lowest between 17.85 and 16.1 ka, and improves by 16 ka due to a 15.4 ka ^{230}Th date and the 16.1 and 14.5 ka tie points with Laura. Following these tie points, the age model until the hiatus at 11.6 ka is established from ^{230}Th tie points, with interpolation between dated points further constrained by counting of 600 annual layers (14.5 to 13.9 ka) during the Bolling-Allerød. This set of speleothem records chronicles the changes across TI in higher detail than previous records from the region, with the following average absolute 95% CI age uncertainties 20–18 ka (Candela, ± 300 years); 18–16 ka (Candela, ± 500 years), 16–14 ka (Laura, ± 150 years); 14–12.5 ka (Candela ± 260 years).

Age models for stalagmites spanning TII and the Bchron uncertainty windows, are illustrated in Supplementary Figs. 5 and 6. For TII, Garth provides anchor chronology due to its high U content and growth rate and presence of annual fluorescent growth banding; Gael also provides an independent chronology albeit of lesser resolution. For Neith, whose very low U content complicates a precise age model, we develop an age model by tuning main features of isotope record to that of Garth within the uncertainties of the Bchron model. Neith is therefore presented to indicate the reproducibility of the main features of the isotopic records shown in Garth, not as independent verification of precise event chronology. The age model in Garth was developed with the aid of laminae counting (Supplementary Fig. 5).

Stable isotope analysis and TI stable isotope splice. New stable isotope determinations were measured at Scientific and Technologic Centers from the University of Barcelona with a Thermo-Finnigan MAT-252 coupled to a CarboKiel-II and at ETH Zürich with a Thermo-Finnigan Delta V Plus coupled to Gas Bench II⁸³ and are reported in ‰ relative to the Vienna PDB Standard. Analytical uncertainties for calibration with two in-house carbonate standards and NBS-19 and NBS-18 international standard and were 0.08 ‰ for both isotopes. Samples for isotopes were micromilled at 0.1 to 0.5 mm increments, or drilled at 1 to 5 mm increments, from the central axis of stalagmites. Stalagmite $\delta^{18}\text{O}$ and $\delta^{13}\text{C}$ were screened for the coupled effects of CO_2 degassing and prior calcite precipitation, as detailed below. A spliced record of $\delta^{18}\text{O}_{\text{NISA}}$ and $\delta^{13}\text{C}_{\text{NISA}}$ is compiled from stalagmites spanning 26–5 ka BP. Where multiple stalagmites grow synchronously, we employ for the splice, the stalagmite with best constrained chronology and the stalagmite in which there is the least variation in $\text{Mg}/\text{Ca}_{\text{index}}$ over the included time interval. The goal of this approach is to limit the potential influence of PCP on the inferred trends in $\delta^{18}\text{O}_{\text{NISA}}$ and $\delta^{13}\text{C}_{\text{NISA}}$.

Speleothem Mg/Ca analysis, Mg/Ca as PCP index, and screening for PCP influence on isotope records. Mg/Ca was measured on splits of the isotope samples, at the University of Oviedo (Thermo ICAP DUO 6300)⁷², and with similar standardization approaches at ETH Zürich (Agilent QQQ 8800); all ratios are reported in mmol/mol. Mg/Ca is widely used indicator of variation in PCP⁸⁴ and we use speleothem Mg/Ca and the $\text{Mg}/\text{Ca}_{\text{index}}$ as a qualitative indicator of the influence of the coupled process of CO_2 degassing and prior calcite precipitation (PCP) on isotope trends, hereafter referred to as PCP. To facilitate comparison across stalagmites from different portions of the cave, which sample stratigraphically distinct portions of the host limestone, we normalize the measured Mg/Ca in each sample ($\text{Mg}/\text{Ca}_{\text{sample}}$) to the minimum Mg/Ca of that stalagmite ($\text{Mg}/\text{Ca}_{\text{min}}$), where high index suggests little loss of Ca due to PCP and a low index suggests significant loss of Ca due to PCP.

$$\text{Mg}/\text{Ca}_{\text{index}} = (\text{Mg}/\text{Ca}_{\text{min}})/(\text{Mg}/\text{Ca}_{\text{sample}}) \quad (1)$$

Since the $\delta^{13}\text{C}$ of dripwater acquired through rain equilibration with soil gas and bedrock dissolution is the primary signal of interest, we plot stalagmite $\delta^{13}\text{C}$ coded by the $\text{Mg}/\text{Ca}_{\text{index}}$ (Supplementary Figs. 4, 8, 10) to identify when there may

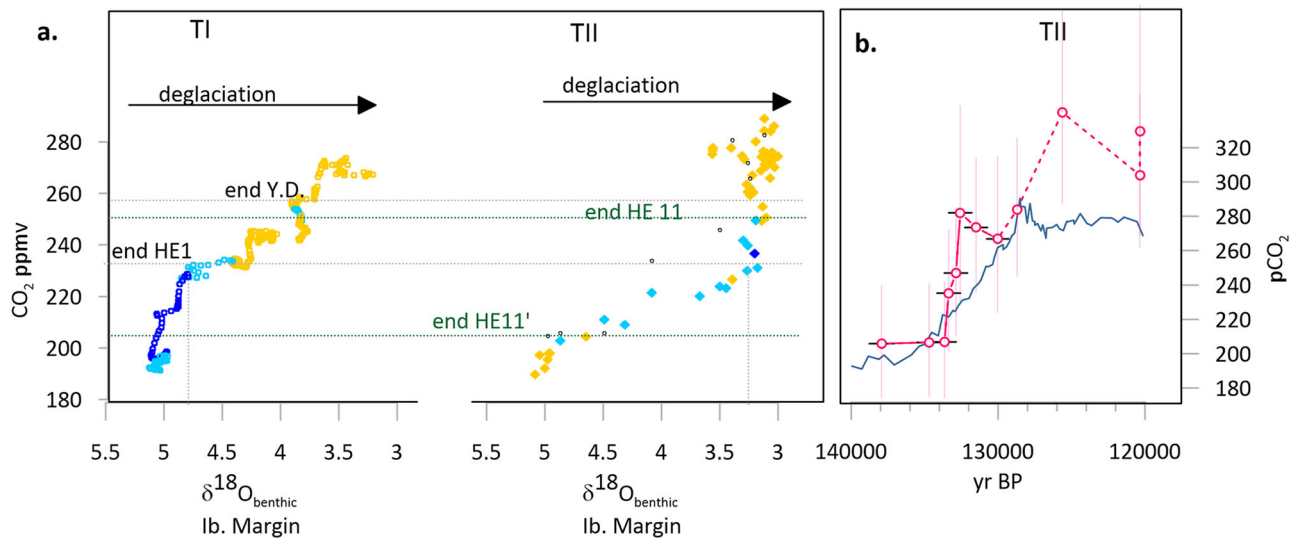


Fig. 8 Evolution of atmospheric pCO₂ during TI and TII. **a** The evolution of ice core pCO₂ for TI⁶⁴ and TII⁷ versus benthic δ¹⁸O on the Iberian margin; benthic δ¹⁸O tuned to speleothem chronology for TII. Symbols are colored according to the C_{37:4} alkenone abundance in the S. Iberian margin⁵⁸ (dark blue C_{37:4} > 6%; light blue C_{37:4} 2–6%; yellow < 2%) as an indicator of timing and intensity of HE climate impact. Horizontal gray lines emphasize CO₂ levels reached following abrupt rises during stadials in TI (HE1 and Y.D.), and horizontal dark green lines highlight CO₂ levels attained at the end of stadials in TII (HE11' and HE11). **b** Comparison of the TII temporal evolution of CO₂ on ice core chronology (gray curve)⁷ with pCO₂ estimated from marine proxies (pink, vertical bars show 95% CI on CO₂ estimate)⁶⁶ on speleothem chronology as discussed in Methods (horizontal bars show ±750 year uncertainty on age). The TII marine proxy pCO₂ estimates from between 138 and 128 ka are shown with small black squares in a), with error bars omitted for clarity.

be an additional component of variation in δ¹³C_{NISA} due to in-cave modification of dripwater δ¹³C due to CO₂ degassing and PCP. Monitoring suggests that secondary factors such as changes in Mg partitioning, non-bedrock Mg sources, and variations in the congruency of bedrock dissolution due to variable water-rock contact times exert a limited influence on speleothem Mg/Ca in most of our studied stalagmites. We refrain from use of the Mg/Ca index, and interpretation of isotope results, for the <9 ka portions of Pindal Cave stalagmites in which the cave position on the sea cliff generates a strong marine aerosol Mg/Ca influence. Based on our finding that in stalagmites spanning TI, the main glacial/interglacial δ¹³C_{NISA} contrasts and main transitions do not coincide with unidirectional changes in Mg/Ca_{index} we conclude these are not artefacts of varying PCP.

In TII, the Mg/Ca_{index} is used to ascertain trends which are not influenced by PCP. In stalagmite Garth, the principal transition to strongly negative δ¹³C_{NISA} 136–130 ka occurs within a very narrow range in Mg/Ca (4.7 ± 0.37 (1 s) mmol/mol) (Supplementary Figs. 8, 10), confirming this δ¹³C_{NISA} transition is not driven by variable PCP. However, Mg/Ca in Garth rises abruptly after 129 ka and between 127 and 122 ka, the coincidence of maximum Mg/Ca ratios and strongly condensed growth indicated by ²³⁰Th ages is most likely explained by enhanced PCP (Supplementary Fig. 10). Between 127 and 122 ka, δ¹³C_{NISA} may be shifted to more positive values than would be attained if PCP values were comparable to other sections of the stalagmite and therefore, PCP may be attenuating the magnitude of change in δ¹³C_{NISA} during peak MIS5e warmth in this stalagmite. Consequently, we rely on other stalagmite record for this interval. Stalagmite Gael, shows overall more constant Mg/Ca_{index} than Garth (Supplementary Fig. 8h), suggesting that relative trends in δ¹³C_{NISA} between early termination (134–130 ka) and peak MIS 5e (127–123 ka) are less influenced by PCP in Gael. At the same time, the trend in δ¹³C_{NISA} at the termination onset may be amplified in Gael by decrease in PCP between 135 and 134 ka. In stalagmite Neith, Mg/Ca and δ¹³C_{NISA} correlate strongly within glacial and termination time windows (Supplementary Fig. 8i) and although a shift in mean δ¹³C_{NISA} between glacial and interglacial is evident, PCP may be the dominant source of temporal variation in δ¹³C_{NISA} within each of these time windows, so we abstain from interpreting the time series of δ¹³C_{NISA} in Neith. We propose stalagmite Garth, with high and relatively stable Mg/Ca_{index} and most precise chronology, to present the most reliable δ¹³C_{NISA} record, except during its condensed interval between 128 and 122 ka; for this latter period, we splice in the temporal variation observed in stalagmite Gael so that long term trends can be accurately assessed.

We also use the Mg/Ca index to evaluate the potential effect of varying PCP on δ¹⁸O, since stalagmite δ¹⁸O may be isotopically enriched when forming from dripwaters which have experienced significant PCP at rates exceeding those of oxygen isotope equilibration between dissolved inorganic carbon and water, as observed in laboratory studies^{85,86}. The magnitude of this effect in cave settings could be buffered by the large water reservoir exchanging with DIC especially if carbonic anhydrase from soil and cave microbial^{87,88} communities catalyzes exchange. Using previously published δ¹⁸O_{NISA} records from 100 to 80 ka²⁷, we

find that a lower Mg/Ca_{index} coincides with stalagmite sections offset to higher δ¹⁸O_{NISA} relative to coeval stalagmites, suggesting this index is useful to identify PCP-related influences on δ¹⁸O_{NISA} in these cave settings (Supplementary Fig. 7).

In stalagmites spanning TI, the major temporal trends in our δ¹⁸O_{NISA} records do not correlate with Mg/Ca_{index} in the intervals of each record selected for the splice (Supplementary Fig. 2). In the spliced record overall, there is no systematic correlation between Mg/Ca_{index} and the decrease in δ¹⁸O. Therefore there is no evidence the δ¹⁸O trends are artefacts of temporally variable PCP.

During TII, we evaluate whether deglacial δ¹⁸O_{NISA} changes coincide with changes in cave-influences (such as PCP) using crossplots of isotopic records with Mg/Ca (Supplementary Fig. 8). We color code data by age. This analysis confirms that in Garth, there is no correlation between Mg/Ca and δ¹⁸O_{NISA}; the full transition of δ¹⁸O_{NISA} from 136 to 132 ka occurs when the speleothem maintains a very narrow range in Mg/Ca (4.8 ± 0.35 (1 s) mmol/mol), suggesting that variation in PCP is not a significant influence on the trend in δ¹⁸O_{NISA} in this time interval. Over the termination there is also no correlation between growth rate and δ¹⁸O_{NISA} in Garth, the stalagmite for which growth rate is most precisely resolved due to annual layer counting. (Supplementary Fig. 8). Although the timing and features of the δ¹⁸O_{NISA} are similar in stalagmite Gael, its δ¹⁸O_{NISA} is on average 1% higher compared to stalagmite Garth or Neith. Gael has a lower average Mg/Ca_{index} than the other two stalagmites, suggestive of greater PCP which could lead to offset of the absolute δ¹⁸O_{NISA} for stalagmite Gael. Additionally in Gael, the shift to slightly lower mean value of Mg/Ca midway through the termination onset coincides with a reduced offset in δ¹⁸O_{NISA} between Gael and Garth (Supplementary Fig. 9), amplifying the δ¹⁸O_{NISA} transition in Gael between 135 and 134 ka by about 0.5%. In Neith, there is no correlation between δ¹⁸O_{NISA} and Mg/Ca, and for Gael and Neith, growth rates are less precisely constrained but there is no consistent correlation between average growth rate and δ¹⁸O_{NISA}. Therefore, we employ stalagmite Garth, with high and relatively stable Mg/Ca_{index} and most precise chronology, as our core δ¹⁸O_{NISA} record, except during its condensed interval between 128 and 122 ka, when the period of most significant PCP may increase the δ¹⁸O_{NISA} compared to other time intervals in that stalagmite. During the interval of condensed growth in Garth, we splice in the temporal variation observed in stalagmite Gael, plotting them on a separate y-axis so that long term trends can be accurately assessed. We employ the record from stalagmite Garth to estimate the eastern North Atlantic surface ocean δ¹⁸O_{sw} anomaly relative to the Iberian margin δ¹⁸O_{benthic} (δ¹⁸O_{NISA-BC}; Methods).

Estimation of δ¹⁸O_{sw} relationship with δ¹⁸O_{NISA} over TI and calculation of surface ocean anomaly. The δ¹⁸O of surface seawater (δ¹⁸O_{sw}) is commonly estimated from coupled Mg/Ca and δ¹⁸O of planktic foraminifera⁸⁹. We compare published marine δ¹⁸O_{sw} with δ¹⁸O_{NISA} over the time interval from 25 to 5 ka BP in fixed 500 year time bins (Fig. 2, Supplementary Fig. 3). The marine records are based on original ¹⁴C chronology which for the S Iberian margin assumes constant

reservoir age¹⁷. For the W Iberian margin we apply recent age model assuming variable reservoir age⁹⁰. For the Irish margin, the original chronology is based on tuning the % *N. pachyderma sinistral* relative abundance to the GISPII $\delta^{18}\text{O}$ variation since ¹⁴C dates suggested variable reservoir age³². Superimposed multi-centennial-scale variability is evident in both $\delta^{18}\text{O}_{\text{sw}}$ and $\delta^{18}\text{O}_{\text{NISA}}$, but at this time cannot be confidently independently correlated due to the uncertainty of marine ¹⁴C-based and correlation-based age models.

The calculation of regional surface ocean $\delta^{18}\text{O}_{\text{sw}}$ anomaly as a surface ocean $\delta^{18}\text{O}_{\text{sw}}$ minus a global $\delta^{18}\text{O}$ “ice volume effect” is subject to uncertainties in the age correlation between the $\delta^{18}\text{O}_{\text{sw}}$ and the eustatic sea level curve used to calculate the ice volume effect. To reduce this source of uncertainty and to use a similar metric for TI and TII, we instead describe the local surface ocean $\delta^{18}\text{O}_{\text{sw}}$ ($\delta^{18}\text{O}_{\text{NISA}}$) relative to the benthic $\delta^{18}\text{O}_{\text{calcite}}$ on the Iberian margin, which can be precisely and independently tuned to speleothem chronology for TII. This metric is denominated ($\delta^{18}\text{O}_{\text{NISA-BC}}$) or ($\delta^{18}\text{O}_{\text{SW-BC}}$). Although the decrease in benthic $\delta^{18}\text{O}_{\text{calcite}}$ is driven by both deep ocean warming and decreasing deep ocean water $\delta^{18}\text{O}$ components, high resolution OA GCM model simulations show that in the depth range of our Iberian Margin North Atlantic records, decreasing deep ocean $\delta^{18}\text{O}$ and warming are closely temporally coupled when meltwater release decreases AMOC intensity, because shallowed North Atlantic winter mixed layer depth lead to mid-depth warming¹¹.

Tuning of marine age models for Iberian Margin to speleothem chronology.

We compile published $\delta^{18}\text{O}_{\text{sw}}$ records for TII^{18,91} based on Mg/Ca SST and $\delta^{18}\text{O}_{\text{calcite}}$ and align the major depletion in both $\delta^{18}\text{O}_{\text{sw}}$ of ODP 977⁹¹ and in $\delta^{18}\text{O}_{\text{NISA}}$ in Garth, as illustrated in Supplementary Fig. 11. Because NW Iberian caves also lie in the center of a broad region affected by pronounced cooling during AMOC weakening events¹⁰, we extend the NW Iberian speleothem chronology by the additional alignment of three key cooling events in the $\delta^{13}\text{C}_{\text{NISA}}$ record with events identified in the alkenone-SST record also from ODP 977⁹². ODP 977 is the primary tuning target because is the only available $\delta^{18}\text{O}_{\text{sw}}$ record that matches exactly the amplitude of the initial speleothem freshening in both TI and TII (Fig. 6; Supplementary Fig. 13), likely because by the strong density gradient between the surface melt waters and the underlying Mediterranean waters maintains strong surface stratification, but also because higher sedimentation rates in ODP 977 may better preserve the original $\delta^{18}\text{O}_{\text{sw}}$ amplitude (Supplementary Fig. 12). The tuning is based on tie points between 135 and 125 ka leading to highest precision in the marine chronology during this tuned interval and we do not discuss the details of marine records prior to MWPTII-B.

The ODP 977 marine chronology is transferred to ODP 976⁹³ on the S Iberian margin and MD01-2444^{18,59} in the W Iberian margin by alignment of five tie points that represent main trends changes in the *G. bulloides* $\delta^{18}\text{O}_{\text{plank}}$ curves (Supplementary Fig. 12) as this species and record has previously been shown to be useful stratigraphical tool in this region to synchronize their signal to Greenland climate evolution^{94–96}. The resulting marine chronologies yield coherent main structures in alkenone-SST records^{92,97} and $\delta^{18}\text{O}_{\text{sw}}$ records^{18,59} of each site (Supplementary Figs. 13 and 14), but $\delta^{18}\text{O}_{\text{sw}}$ on the W Iberian Margin (MD01-2444) is somewhat attenuated, potentially due to low biogenic productivity and foraminiferal growth periods which are biased against extreme conditions^{96,98}.

Tuning of bipolar-polar North Atlantic marine age models for Iberian Margin to speleothem chronology.

For ODP 983⁹⁹ and 984¹⁰⁰ we align the major reduction in %*N. pachyderma sinistral* with the deglacial temperature rise in the Alkenone SST record from ODP 977, a clear structure that correlates well all along the Iberian margin cores, as well as a subsequent local maximum in %*N. pachyderma sinistral* evident as a local minimum in alkenone SST (Supplementary Fig. 14). The strategy is based on the synchronicity of millennial scale cooling events resulting from AMOC reorganization, widely used to apply an Antarctic or synthetic Greenland chronology to marine records⁹⁹. Our tuning is consistent with $\delta^{18}\text{O}_{\text{plank}}$ and IRD records (Supplementary Fig. 14). We align the Eirik Drift core MD03-2664^{101,102} by correlating two major structures in the %*N. pachyderma sinistral* with ODP 984 (Supplementary Fig. 14), which results in end of IRD deposition nearly synchronous with the other N Atlantic sites. The $\delta^{18}\text{O}_{\text{sw}}$ at this location should have a strong regional signature of the NAIS melting through the Labrador Sea, and the major melting is observed after the main NE Atlantic freshening as recorded in the NW Iberian $\delta^{18}\text{O}_{\text{NISA}}$ (Supplementary Fig. 13), but coincident with one of the minor freshening structures of the NISA record at the onset of the MIS 5e and with comparable amplitude. The benthic record $\delta^{18}\text{O}_{\text{benthic}}$ at these shallow N Atlantic sites (e.g., 984 1650 m, 983 1985 m) is known to lead that of deep N Atlantic and S Atlantic and Pacific over the TI¹⁰³ and the applied tuning suggests a similar pattern in the TII (Supplementary Fig. 15).

Within H11, we have not relied on temperature records for tuning, because the alkenone temperatures exhibit a slower rate of warming than implied by $\delta^{13}\text{C}_{\text{NISA}}$. Additionally, compared to alkenones, Mg/Ca SST records from the same cores (not shown)^{18,91,93} exhibit divergent millennial structure and amplitude of SST change across H11 likely reflecting a seasonality control in the H11 temperature signal. More intense winter cooling but summer warming¹⁰⁴ during cold reversals may lead to differences in rate of winter vs annual or summer warming, which may enhance discrepancies among proxies which may have differing influence of

summer and winter seasons. An additional factor which has been documented to slow the manifestation of deglacial SST rise in alkenone records on the Iberian Margin is the transport of glacial-aged alkenones into sediments of deglacial and early interglacial age²⁹.

Tuning of Western Caribbean marine age models for Iberian Margin to speleothem chronology.

We tune ODP 999 using its $\delta^{18}\text{O}_{\text{sw}}$ record during the termination and using its $\delta^{18}\text{O}_{\text{planktic}}$ record during the interglacial. $\delta^{18}\text{O}_{\text{sw}}$ tuning of TII is based on observed lags during TI. During TI, the $\delta^{18}\text{O}_{\text{sw}}$ of ODP 999⁶⁷ is based on 14 C age model, updated to INTCAL2013 with constant 400 year reservoir age. During TI the W Iberian margin $\delta^{18}\text{O}_{\text{benthic}}$ ¹⁰⁵ is on chronology tuned to GRIP¹⁰⁶ and Hulu⁹⁰. We observe that depletion of $\delta^{18}\text{O}_{\text{sw}}$ at ODP 999 lags that of W Iberian margin $\delta^{18}\text{O}_{\text{benthic}}$ by an average of 1100 years (Supplementary Fig. 17a). This lag is consistent with timescales of ocean mixing required to distribute the ice volume signal¹⁰⁷. Therefore the same lag is used on TII to align the $\delta^{18}\text{O}_{\text{sw}}$ and W Iberian margin $\delta^{18}\text{O}_{\text{benthic}}$ ¹⁰⁵ and assign chronology to ODP 999. We do not use the 999 $\delta^{18}\text{O}_{\text{planktic}}$ for tuning during the termination because during the phase of meltwater addition, $\delta^{18}\text{O}_{\text{planktic}}$ would be expected to have contrasting temperature components on the Iberian margin (strong cooling linked to AMOC shutdown) and western Caribbean (no cooling from AMOC shutdown). However, during the interglacial, these two subtropical locations may be expected to have similar evolution of SST and $\delta^{18}\text{O}_{\text{sw}}$. Therefore we use the combined signal of $\delta^{18}\text{O}_{\text{planktic}}$ to serve directly for correlation during MIS 5e (Supplementary Fig. 17b).

Estimation of terrestrial and marine components of the PGM EIS.

We approximate the ‘marine’ proportion of the T1 and T2 Eurasian ice sheet using the ice sheet reconstructions of^{16,61} and an ice history that is the same as ICE6G for T2¹⁰⁸. The sea level history and glacial isostatic adjustment modelling is from⁸, using the same ice sheet histories. ‘Marine’ ice is defined here simply as the volume of ice that is grounded below the reconstructed sea level.

Reporting summary. Further information on research design is available in the Nature Research Reporting Summary linked to this article.

Data availability

The absolute U-Series and Radiocarbon dates are provided in the Supplementary Information. The Speleothem stable isotope data and interpolated ages are submitted to the SISAL database, and additionally are available from the ETH Research data archive at doi: 10.3929/ethz-b-000545925.

Received: 4 March 2022; Accepted: 27 June 2022;

Published online: 02 July 2022

References

- DeConto, R. M. & Pollard, D. Contribution of Antarctica to past and future sea-level rise. *Nature* **531**, 591–597 (2016).
- Gregoire, L. J., Payne, A. J. & Valdes, P. J. Deglacial rapid sea level rises caused by ice-sheet saddle collapses. *Nature* **487**, 219–222 (2012).
- Shakun, J. D. et al. Global warming preceded by increasing carbon dioxide concentrations during the last deglaciation. *Nature* **484**, 49 (2012).
- Cheng, H. et al. Ice age terminations. *Science* **326**, 248–252 (2009).
- Barker, S. & Knorr, G. Millennial scale feedbacks determine the shape and rapidity of glacial termination. *Nat. Commun.* **12**, 1–12 (2021).
- Dyer, B. et al. Sea-level trends across The Bahamas constrain peak last interglacial ice melt. *Proc. Natl. Acad. Sci.* **118**, 1–11 (2021).
- Köhler, P., Nehrass-Ahles, C., Schmitt, J., Stocker, T. F. & Fischer, H. A 156 kyr smoothed history of the atmospheric greenhouse gases CO₂, CH₄, and N₂O and their radiative forcing. *Earth Syst. Sci. Data* **9**, 363–387 (2017).
- Dendy, S., Austermann, J., Creveling, J. & Mitrovica, J. Sensitivity of Last Interglacial sea-level high stands to ice sheet configuration during Marine Isotope Stage 6. *Quat. Sci. Rev.* **171**, 234–244 (2017).
- Clark, P. U. et al. Oceanic forcing of penultimate deglacial and last interglacial sea-level rise. *Nature* **577**, 660–664 (2020).
- Ivanovic, R. et al. Acceleration of northern ice sheet melt induces AMOC slowdown and northern cooling in simulations of the early last deglaciation. *Paleoceanogr. Paleoclimatol.* **33**, 807–824 (2018).
- Zhang, J. et al. Asynchronous warming and $\delta^{18}\text{O}$ evolution of deep Atlantic water masses during the last deglaciation. *Proc. Natl. Acad. Sci.* **114**, 11075–11080 (2017).
- Wickert, A. D., Mitrovica, J. X., Williams, C. & Anderson, R. S. Gradual demise of a thin southern Laurentide ice sheet recorded by Mississippi drainage. *Nature* **502**, 668 (2013).

13. Keigwin, L. D. et al. Deglacial floods in the beaufort sea preceded younger dryas cooling. *Nat. Geosci.* **11**, 599 (2018).
14. Eynaud, F. et al. New constraints on European glacial freshwater releases to the North Atlantic Ocean. *Geophys. Res. Lett.* **39**, 1–6 (2012).
15. Baker, A. et al. Global analysis reveals climatic controls on the oxygen isotope composition of cave drip water. *Nat. Commun.* **10**, 1–7 (2019).
16. Peck, V. L., Hall, I. R., Zahn, R. & Elderfield, H. Millennial-scale surface and subsurface paleothermometry from the northeast Atlantic, 55–8 ka BP. *Paleoceanography* **23**, 1–11 (2008).
17. Català, A., Cacho, I., Frigola, J., Pena, L. D. & Lirer, F. Holocene hydrography evolution in the Alboran Sea: a multi-record and multi-proxy comparison. *Climate* **15**, 927–942 (2019).
18. Skinner, L. & Shackleton, N. Deconstructing Terminations I and II: Revisiting the glacioeustatic paradigm based on deep-water temperature estimates. *Quat. Sci. Rev.* **25**, 3312–3321 (2006).
19. Vargas-Yáñez, M. et al. About the seasonal variability of the Alboran Sea circulation. *J. Mar. Syst.* **35**, 229–248 (2002).
20. Bigg, G. et al. Sensitivity of the North Atlantic circulation to break-up of the marine sectors of the NW European ice sheets during the last glacial: A synthesis of modelling and palaeoceanography. *Glob. Planet. Change* **98**, 153–165 (2012).
21. Zanchetta, G. et al. Coeval dry events in the central and eastern Mediterranean basin at 5.2 and 5.6 ka recorded in Corchia (Italy) and Soreq caves (Israel) speleothems. *Glob. Planet. Change* **122**, 130–139 (2014).
22. Bajo, P. et al. Persistent influence of obliquity on ice age terminations since the Middle Pleistocene transition. *Science* **367**, 1235–1239 (2020).
23. Drysdale, R. et al. Evidence for obliquity forcing of glacial termination II. *Science* **325**, 1527–1531 (2009).
24. McDermott, F., Atkinson, T., Fairchild, I. J., Baldini, L. M. & Matthey, D. P. A first evaluation of the spatial gradients in $\delta^{18}\text{O}$ recorded by European Holocene speleothems. *Glob. Planet. Change* **79**, 275–287 (2011).
25. Moseley, G. E. et al. Multi-speleothem record reveals tightly coupled climate between central Europe and Greenland during Marine Isotope Stage 3. *Geology* **42**, 1043–1046 (2014).
26. Koltai, G. et al. A penultimate glacial climate record from southern Hungary. *J. Quat. Sci.* **32**, 946–956 (2017).
27. Stoll, H. et al. Interpretation of orbital scale variability in mid-latitude speleothem $\delta^{18}\text{O}$: Significance of growth rate controlled kinetic fractionation effects. *Quat. Sci. Rev.* **127**, 215–228 (2015).
28. Skinner, L. C., Waelbroeck, C., Scrivner, A. E. & Fallon, S. J. Radiocarbon evidence for alternating northern and southern sources of ventilation of the deep Atlantic carbon pool during the last deglaciation. *Proc. Natl Acad. Sci.* **111**, 5480–5484 (2014).
29. Ausin, B. et al. (In) coherent multiproxy signals in marine sediments: Implications for high-resolution paleoclimate reconstruction. *Earth Planet. Sci. Lett.* **515**, 38–46 (2019).
30. Genty, D. et al. Precise dating of Dansgaard-Oeschger climate oscillations in western Europe from stalagmite data. *Nature* **421**, 833–837 (2003).
31. Lechleitner, F. A. et al. Stalagmite carbon isotopes suggest deglacial increase in soil respiration in western Europe driven by temperature change. *Clim. Past* **17**, 1903–1918 (2021).
32. Peck, V. L. et al. High resolution evidence for linkages between NW European ice sheet instability and Atlantic Meridional Overturning Circulation. *Earth Planet. Sci. Lett.* **243**, 476–488 (2006).
33. Nicholl, J. A. et al. A Laurentide outburst flooding event during the last interglacial period. *Nat. Geosci.* **5**, 901 (2012).
34. Tarasov, L., Dyke, A. S., Neal, R. M. & Peltier, W. R. A data-calibrated distribution of deglacial chronologies for the North American ice complex from glaciological modeling. *Earth Planet. Sci. Lett.* **315**, 30–40 (2012).
35. Lisiecki, L. E. & Raymo, M. E. A Pliocene-Pleistocene stack of 57 globally distributed benthic $\delta^{18}\text{O}$ records. *Paleoceanography* **20**, 1–17 (2005).
36. Düsterhus, A., Tamisieva, M. E. & Jevrejeva, S. Estimating the sea level highstand during the last interglacial: a probabilistic massive ensemble approach. *Geophys. J. Int.* **206**, 900–920 (2016).
37. Waelbroeck, C. et al. Sea-level and deep water temperature changes derived from benthic foraminifera isotopic records. *Quat. Sci. Rev.* **21**, 295–305 (2002).
38. Grant, K. et al. Rapid coupling between ice volume and polar temperature over the past 150,000 years. *Nature* **491**, 744 (2012).
39. Grant, K. et al. Sea-level variability over five glacial cycles. *Nat. Commun.* **5**, 5076 (2014).
40. Marino, G. et al. Bipolar seesaw control on last interglacial sea level. *Nature* **522**, 197 (2015).
41. Yokoyama, Y. et al. Rapid glaciation and a two-step sea level plunge into the Last Glacial Maximum. *Nature* **559**, 603–607 (2018).
42. Roche, D. M., Wiersma, A. P. & Renssen, H. A systematic study of the impact of freshwater pulses with respect to different geographical locations. *Clim. Dyn.* **34**, 997–1013 (2010).
43. Roche, D. M., Paillard, D., Caley, T. & Waelbroeck, C. LGM hosing approach to Heinrich Event 1: results and perspectives from data–model integration using water isotopes. *Quat. Sci. Rev.* **106**, 247–261 (2014).
44. Svendsen, J. I. et al. Late Quaternary ice sheet history of northern Eurasia. *Quat. Sci. Rev.* **23**, 1229–1271 (2004).
45. Rohling, E. J. et al. Differences between the last two glacial maxima and implications for ice-sheet, $\delta^{18}\text{O}$, and sea-level reconstructions. *Quat. Sci. Rev.* **176**, 1–28 (2017).
46. Colleoni, F., Wekerle, C., Näslund, J.-O., Brandefelt, J. & Masina, S. Constraint on the penultimate glacial maximum Northern Hemisphere ice topography (≈ 140 kyrs BP). *Quat. Sci. Rev.* **137**, 97–112 (2016).
47. Stein, R., Fahl, K., Gierz, P., Niessen, F. & Lohmann, G. Arctic Ocean sea ice cover during the penultimate glacial and the last interglacial. *Nat. Commun.* **8**, 1–13 (2017).
48. Jakobsson, M. et al. Evidence for an ice shelf covering the central Arctic Ocean during the penultimate glaciation. *Nat. Commun.* **7**, 1–10 (2016).
49. Geibert, W., Matthiessen, J., Stimac, I., Wollenburg, J. & Stein, R. Glacial episodes of a freshwater Arctic Ocean covered by a thick ice shelf. *Nature* **590**, 97–102 (2021).
50. Gherardi, J.-M. et al. Evidence from the Northeastern Atlantic basin for variability in the rate of the meridional overturning circulation through the last deglaciation. *Earth Planet. Sci. Lett.* **240**, 710–723 (2005).
51. Bradtmiller, L. I., McManus, J. F. & Robinson, L. F. 231 Pa/230 Th evidence for a weakened but persistent Atlantic meridional overturning circulation during Heinrich Stadial 1. *Nat. Commun.* **5**, 1–8 (2014).
52. Condron, A. & Winsor, P. Meltwater routing and the Younger Dryas. *Proc. Natl Acad. Sci.* **109**, 19928–19933 (2012).
53. He, C. et al. North Atlantic subsurface temperature response controlled by effective freshwater input in “Heinrich” events. *Earth Planet. Sci. Lett.* **539**, 116247 (2020).
54. Alvarez-Solas, J., Robinson, A., Montoya, M. & Ritz, C. Iceberg discharges of the last glacial period driven by oceanic circulation changes. *Proc. Natl Acad. Sci.* **110**, 16350–16354 (2013).
55. McManus, J. F., Oppo, D. W. & Cullen, J. L. A 0.5-million-year record of millennial-scale climate variability in the North Atlantic. *Science* **283**, 971–975 (1999).
56. Barker, S. et al. Early interglacial legacy of deglacial climate instability. *Paleoceanogr. Paleoclimatol.* **34**, 1455–1475 (2019).
57. Wang, K. J. et al. Group 2i Isochrystidales produce characteristic alkenones reflecting sea ice distribution. *Nat. Commun.* **12**, 1–10 (2021).
58. Martrat, B. et al. Four climate cycles of recurring deep and surface water destabilizations on the Iberian margin. *Science* **317**, 502–507 (2007).
59. Tzedakis, P. et al. Enhanced climate instability in the North Atlantic and southern Europe during the Last Interglacial. *Nat. Commun.* **9**, 4235 (2018).
60. Peyaud, V. *Rôle de la dynamique des calottes glaciaires dans les grands changements climatiques des périodes glaciaires-interglaciaires*, (2006).
61. Lambeck, K. et al. Constraints on the Late Saalian to early Middle Weichselian ice sheet of Eurasia from field data and rebound modelling. *Boreas* **35**, 539–575 (2006).
62. Obase, T. & Abe-Ouchi, A. Abrupt Bølling-Allerød warming simulated under gradual forcing of the last deglaciation. *Geophys. Res. Lett.* **46**, 11397–11405 (2019).
63. Liakka, J., Löfverström, M. & Colleoni, F. The impact of the North American glacial topography on the evolution of the Eurasian ice sheet over the last glacial cycle. *Climate* **12**, 1225–1241 (2016).
64. Marcott, S. A. et al. Centennial-scale changes in the global carbon cycle during the last deglaciation. *Nature* **514**, 616–619 (2014).
65. Suwa, M. & Bender, M. L. Chronology of the Vostok ice core constrained by O₂/N₂ ratios of occluded air, and its implication for the Vostok climate records. *Quat. Sci. Rev.* **27**, 1093–1106 (2008).
66. Chalk, T. B. et al. Causes of ice age intensification across the Mid-Pleistocene Transition. *Proc. Natl Acad. Sci.* **114**, 13114–13119 (2017).
67. Schmidt, M. W., Spero, H. J. & Lea, D. W. Links between salinity variation in the Caribbean and North Atlantic thermohaline circulation. *Nature* **428**, 160 (2004).
68. Gomez, N., Weber, M. E., Clark, P. U., Mitrovica, J. X. & Han, H. K. Antarctic ice dynamics amplified by Northern Hemisphere sea-level forcing. *Nature* **587**, 600–604 (2020).
69. Draxler, R. & Rolph, G. HYSPLIT (HYbrid Single-Particle Lagrangian Integrated Trajectory) model access via NOAA ARL READY website (<http://ready.arl.noaa.gov/HYSPLIT.php>), NOAA Air Resources Laboratory. *Silver Spring, MD* **8**, 26 (2010).
70. Baldini, L. M., McDermott, F., Baldini, J. U., Fischer, M. J. & Möllhoff, M. An investigation of the controls on Irish precipitation $\delta^{18}\text{O}$ values on monthly and event timescales. *Clim. Dyn.* **35**, 977–993 (2010).
71. Stoll, H. M. et al. Paleoclimate and growth rates of speleothems in the northwestern Iberian Peninsula over the last two glacial cycles. *Quat. Res.* **80**, 284–290 (2013).

72. Moreno, A. et al. A speleothem record of glacial (25–11.6 kyr BP) rapid climatic changes from northern Iberian Peninsula. *Glob. Planet. Change* **71**, 218–231 (2010).
73. Romanov, D., Kaufmann, G. & Dreybrodt, W. Modeling stalagmite growth by first principles of chemistry and physics of calcite precipitation. *Geochimica et Cosmochimica Acta* **72**, 423–437 (2008).
74. Sliwinski, J. & Stoll, H. Combined fluorescence imaging and LA-ICP-MS trace element mapping of stalagmites: Microfabric identification and interpretation. *Chem. Geol.* 120397, 1–15 (2021).
75. McGarry, S. F. & Baker, A. Organic acid fluorescence: Applications to speleothem palaeoenvironmental reconstruction. *Quat. Sci. Rev.* **19**, 1087–1101 (2000).
76. Cheng, H. et al. Improvements in ^{230}Th dating, ^{230}Th and ^{234}U half-life values, and U–Th isotopic measurements by multi-collector inductively coupled plasma mass spectrometry. *Earth Planet. Sci. Lett.* **371**, 82–91 (2013).
77. Shen, C.-C. et al. Uranium and thorium isotopic and concentration measurements by magnetic sector inductively coupled plasma mass spectrometry. *Chem. Geol.* **185**, 165–178 (2002).
78. Wacker, L., Lippold, J., Molnár, M. & Schulz, H. Towards radiocarbon dating of single foraminifera with a gas ion source. *Nucl. Instrum. Methods Phys. Res. Sect. B: Beam Interact. Mater. At.* **294**, 307–310 (2013).
79. Reimer, P. J. et al. The IntCal20 Northern Hemisphere radiocarbon age calibration curve (0–55 cal kBP). *Radiocarbon* **62**, 725–757 (2020).
80. Kaal, J. et al. Long-term deforestation in NW Spain: Linking the Holocene fire history to vegetation change and human activities. *Quat. Sci. Rev.* **30**, 161–175 (2011).
81. Parnell, A. & Parnell, M. A. Package ‘Bchron’. (2018).
82. Parnell, A. C., Haslett, J., Allen, J. R., Buck, C. E. & Huntley, B. A flexible approach to assessing synchronicity of past events using Bayesian reconstructions of sedimentation history. *Quat. Sci. Rev.* **27**, 1872–1885 (2008).
83. Breitenbach, S. F. & Bernasconi, S. M. Carbon and oxygen isotope analysis of small carbonate samples (20 to 100 μg) with a GasBench II preparation device. *Rapid Commun. Mass Spectrom.* **25**, 1910–1914 (2011).
84. Fairchild, I. J. & Treble, P. C. Trace elements in speleothems as recorders of environmental change. *Quat. Sci. Rev.* **28**, 449–468 (2009).
85. Polag, D. et al. Stable isotope fractionation in speleothems: Laboratory experiments. *Chem. Geol.* **279**, 31–39 (2010).
86. Riechelmann, D. F. et al. Disequilibrium carbon and oxygen isotope fractionation in recent cave calcite: Comparison of cave precipitates and model data. *Geochimica et Cosmochimica Acta* **103**, 232–244 (2013).
87. Sauze, J., Jones, S. P., Wingate, L., Wohl, S. & Ogée, J. The role of soil pH on soil carbonic anhydrase activity. *Biogeosciences* **15**, 597–612 (2018).
88. Wingate, L. et al. The impact of soil microorganisms on the global budget of $\delta^{18}\text{O}$ in atmospheric CO_2 . *Proc. Natl Acad. Sci.* **106**, 22411–22415 (2009).
89. Lea, D. W. In *The Oceans and Marine Geochemistry*. (ed H. Elderfield) 365–390 (Elsevier-Pergamon, 2003).
90. Freeman, E., Skinner, L., Waelbroeck, C. & Hodell, D. Radiocarbon evidence for enhanced respired carbon storage in the Atlantic at the Last Glacial Maximum. *Nat. Commun.* **7**, 11998 (2016).
91. Torner, J. et al. Ocean-atmosphere interconnections from the last interglacial to the early glacial: An integration of marine and cave records in the Iberian region. *Quat. Sci. Rev.* **226**, 106037 (2019).
92. Martrat, B. et al. Abrupt temperature changes in the Western Mediterranean over the past 250,000 years. *Science* **306**, 1762–1765 (2004).
93. Jiménez-Amat, P. & Zahn, R. Offset timing of climate oscillations during the last two glacial-interglacial transitions connected with large-scale freshwater perturbation. *Paleoceanography* **30**, 768–788 (2015).
94. Shackleton, N. J., Hall, M. A. & Vincent, E. Phase relationships between millennial-scale events 64,000–24,000 years ago. *Paleoceanography* **15**, 565–569 (2000).
95. Cacho, I. et al. Dansgaard-Oeschger and Heinrich event imprints in Alboran Sea paleotemperatures. *Paleoceanography* **14**, 698–705 (1999).
96. Salgueiro, E. et al. Temperature and productivity changes off the western Iberian margin during the last 150 ky. *Quat. Sci. Rev.* **29**, 680–695 (2010).
97. Martrat, B., Jiménez-Amat, P., Zahn, R. & Grimalt, J. O. Similarities and dissimilarities between the last two deglaciations and interglaciations in the North Atlantic region. *Quat. Sci. Rev.* **99**, 122–134 (2014).
98. Ausin, B., Hodell, D. A., Cutmore, A. & Eglinton, T. I. The impact of abrupt deglacial climate variability on productivity and upwelling on the southwestern Iberian margin. *Quat. Sci. Rev.* **230**, 106139 (2020).
99. Barker, S. et al. 800,000 years of abrupt climate variability. *Science* **334**, 347–351 (2011).
100. Mokeddem, Z., McManus, J. F. & Oppo, D. W. Oceanographic dynamics and the end of the last interglacial in the subpolar North Atlantic. *Proc. Natl Acad. Sci.* **111**, 11263–11268 (2014).
101. Irvani, N. et al. Rapid switches in subpolar North Atlantic hydrography and climate during the Last Interglacial (MIS 5e). *Paleoceanography* **27**, 1–16 (2012).
102. Irvani, N. et al. Evidence for regional cooling, frontal advances, and East Greenland Ice Sheet changes during the demise of the last interglacial. *Quat. Sci. Rev.* **150**, 184–199 (2016).
103. Lisiecki, L. E. & Stern, J. V. Regional and global benthic $\delta^{18}\text{O}$ stacks for the last glacial cycle. *Paleoceanography* **31**, 1368–1394 (2016).
104. Schenk, F. et al. Warm summers during the Younger Dryas cold reversal. *Nat. Commun.* **9**, 1–13 (2018).
105. Skinner, L., Elderfield, H. & Hall, M. Phasing of millennial climate events and Northeast Atlantic deep-water temperature change since 50 ka BP. *Wash. DC Am. Geophys. Union Geophys. Monogr. Ser.* **173**, 197–208 (2007).
106. Hodell, D. et al. Response of Iberian Margin sediments to orbital and suborbital forcing over the past 420 ka. *Paleoceanography* **28**, 185–199 (2013).
107. Stern, J. V. & Lisiecki, L. E. Termination 1 timing in radiocarbon-dated regional benthic $\delta^{18}\text{O}$ stacks. *Paleoceanography* **29**, 1127–1142 (2014).
108. Peltier, W. R., Argus, D. & Drummond, R. Space geodesy constrains ice age terminal deglaciation: The global ICE-6G_C (VM5a) model. *J. Geophys. Res.: Solid Earth* **120**, 450–487 (2015).
109. Barker, S. et al. Icebergs not the trigger for North Atlantic cold events. *Nature* **520**, 333 (2015).
110. Skinner, L. & Shackleton, N. Rapid transient changes in northeast Atlantic deep water ventilation age across Termination I. *Paleoceanography* **19**, 1–11 (2004).
111. Carlson, A. E., Clark, P. U., Haley, B. A. & Klinkhammer, G. P. Routing of western Canadian Plains runoff during the 8.2 ka cold event. *Geophys. Res. Lett.* **36**, 1–5 (2009).

Acknowledgements

We thank student assistants Raquel Rodriguez-Francos, Tim Loeffel, Romain Alosius, and Pien Antjewierden for assistance with drilling, and Joaquin Perona (CCiT-UB) and Madalina Jaggi (ETH) for assistance with stable isotope and trace element analyses. We thank staff at Scientific Center for Optical and Electron Microscopy (ScopeM) at ETH Zürich for support for Confocal imaging and Hongrui Zhang for support in processing of climate model output. We thank J. Zhang for provision of the TRACE-21 POP2 model output, and Andrea Burke and James Rae for discussions. We thank Jacky Austermann and Sarah Dendy for providing the relative sea level data.

Author contributions

Interpretations and manuscript writing was carried out by HS, IC and EG with input from all authors. HS initiated the study and led the speleothem interpretations, IC led the interpretation of $\delta^{18}\text{O}_{\text{sw}}$ records and marine tuning, and EG led interpretation of ice sheet history. U–Th chronology was conducted by HS, AM, CP, and MI with support from HC and RLE. Laminae counting and its integration in TII age model development was led by JS. 14 C chronology was completed by NH and OK; OK led TI chronology revision and increased data resolution. Modern rainfall monitoring and HYSPLITT was conducted by MI and new $\delta^{18}\text{O}_{\text{sw}}$ records were produced by JT.

Funding

The research was funded by HIDROPAST (CGL2010-16376) OPERA (CTM2013-48639-C2-1-R) and CHIMERA (CTM2016-75411-R) all to HMS, IC, and AM, and ETH core funding to HS. JT and MI were funded by doctoral FPI fellowships of CTM2013-48639-C2-1-R, and OK by doctoral Fellowship ETH-13 18-1. CP and HC acknowledge NSF Grant 41888101, AM acknowledges CGL2016-77479-R, and RLE acknowledges NSF 1702816 and the 111 program of China grant D19002. IC and JT acknowledge Generalitat de Catalunya Grups de Recerca Consolidats grant 2017 SGR 315 to GRC Geociències Marines, and IC acknowledges the ICREA-Academia programme from the Generalitat de Catalunya and PID2019-105523RB-I00. EG is funded by a Royal Society University Research Fellowship (R1/180317). Samples used in this study were collected in accordance with governing regulations.

Competing interests

The authors declare no competing interests.

Additional information

Supplementary information The online version contains supplementary material available at <https://doi.org/10.1038/s41467-022-31619-3>.

Correspondence and requests for materials should be addressed to Heather M. Stoll.

Peer review information *Nature Communications* thanks the anonymous reviewers for their contribution to the peer review of this work.

Reprints and permission information is available at <http://www.nature.com/reprints>

Publisher's note Springer Nature remains neutral with regard to jurisdictional claims in published maps and institutional affiliations.



Open Access This article is licensed under a Creative Commons Attribution 4.0 International License, which permits use, sharing, adaptation, distribution and reproduction in any medium or format, as long as you give appropriate credit to the original author(s) and the source, provide a link to the Creative Commons license, and indicate if changes were made. The images or other third party material in this article are included in the article's Creative Commons license, unless indicated otherwise in a credit line to the material. If material is not included in the article's Creative Commons license and your intended use is not permitted by statutory regulation or exceeds the permitted use, you will need to obtain permission directly from the copyright holder. To view a copy of this license, visit <http://creativecommons.org/licenses/by/4.0/>.

© The Author(s) 2022